G-APD arrays and their use in axial PET modules

Master Thesis

Author(s):
Krähenbühl, Thomas

Publication date:
2008

Permanent link:
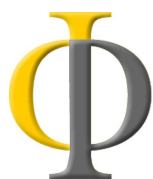https://doi.org/10.3929/ethz-a-007636145

Rights / license:
In Copyright - Non-Commercial Use Permitted

Diploma thesis

G-APD arrays and their use in axial PET modules

Thomas Krähenbühl

August 2008

Final version

European Organization for Nuclear Research (CERN), Geneva
Prof. Felicitas Pauss, ETH Zurich

Abstract

New technical developments allow to build improved detectors for medical applications. AX-PET is a project of the European Organization for Nuclear Research CERN with the aim to build detector modules for positron emission tomography (PET) with significantly improved performance.

One of the central components of AX-PET modules are Geiger-mode avalanche photodiodes (G-APDs) which replace the normally used photomultiplier tubes. The basic properties of G-APDs and a calculation model for the interpretation of measurements which use G-APDs are presented in the first chapter. The second chapter presents experimental methods to measure the parameters for the calculation such as crosstalk and afterpulses.

An introduction to PET and the modifications in AX-PET are found in the third chapter. The energy resolution for 511-keV photons was measured at $11.4\,\%$ using G-APDs on LYSO crystals. The number of detected optical photons in a G-APD for such an event is 1300. The z-coordinate in the direction of the crystals is determined using wavelength shifting (WLS) strips which absorb a part of the light from the crystal. Again G-APDs are used to measure the light yield of the WLS strips. The number of detected photons is 96. The distribution of the light on the WLS strips is examined. The distribution is approximately Gaussian with a full width at half maximum (FWHM) of $3.5\,\text{mm}$. The measurements on the precision of the z-axis readout were non-conclusive.

Not part of this thesis are measurements which were not completed during the author's time at CERN, in particular concerning the timing properties and shape of G-APD signals. Also omitted are topics which are only remotely connected to G-APDs and AX-PET such as the setup of the VME controller and the programming of a C-library for the communication with Caen V792 modules.

Contents

1 Geiger-mode avalanche photodiodes

1.1 Introduction

Geiger-mode avalanche photodiodes (G-APDs) are a new type of semiconductor photodetectors. Though the first devices were already built more than ten years ago, the interest of research groups came only with the commercial availability in the past few years. G-APDs feature outstanding qualities compared to other photodetectors such as high quantum efficiency, low noise, high internal gain and insensibility to magnetic fields. These properties make them an interesting device for a wide range of applications from high energy physics to astronomy or medical applications such as combined PET-MRI scanners.

1.2 Functional principle

A Geiger-mode avalanche photodiode consists of a semiconductor with several variably doped layers. A voltage is applied in vertical direction. Below the so-called breakdown voltage the diode does not operate in Geiger-mode, the occuring processes are as in an avalanche photodiode (APD): a photon hitting the diode creates an electron-hole pair with a certain probability called quantum efficiency (QE). The quantum efficiency depends on the wavelength λ of the incoming photon. Due to the applied voltage, the electron is accelerated and drifts to the p-n junction, releasing secondary electrons through ionization (figure 1). These electrons release further electrons themselves, an avalanche builds up. The initial hole undergoes the same process in the opposite direction. The ionization probability of holes is significantly smaller than for electrons such that only few holes ionize and start new avalanches.

The extent of the avalanche depends on the applied bias voltage V_b. Below the breakdown voltage V_{br}, the number of electrons per initial electron-hole pair grows exponentially with the bias voltage.[1] The ratio of released electrons per initial electron-hole pair is the gain. The gain of an APD is about 1-2000. Multiple photons arriving on the diode at the same time can initiate multiple avalanches and linearly increase the total number of avalanche electrons.

The ionization coefficients of electrons and holes increase with larger bias voltages. Above the breakdown voltage the ionization coefficients are large enough such that the process of holes starting new avalanches becomes self-perpetuating. The avalanche starts itself over and over again in a process called breakdown. The breakdown is only stopped by lowering the bias voltage below the breakdown voltage. This so-called quenching can be done either actively by lowering the applied voltage when a breakdown is detected or passively through a resistor. This operation principle of a diode is called Geiger-mode. The total charge released during breakdown is independent of the initial number of electron-hole pairs. Multiple photons initiating a breakdown cannot be distinguished from a single initial photon. In modern G-APDs the chip area is divided into cells with a cell density of $100 - 10000\,\text{cells/mm}^2$. The cells are connected in parallel to a common voltage supply. Each single cell is operated in Geiger-mode and has an individual quenching resistor.[1] Since all cells produce the same output signal, the comparison of the summed signal to the single cell signal allows calculating the number of cells with a breakdown and by this the intensity of the light flash.
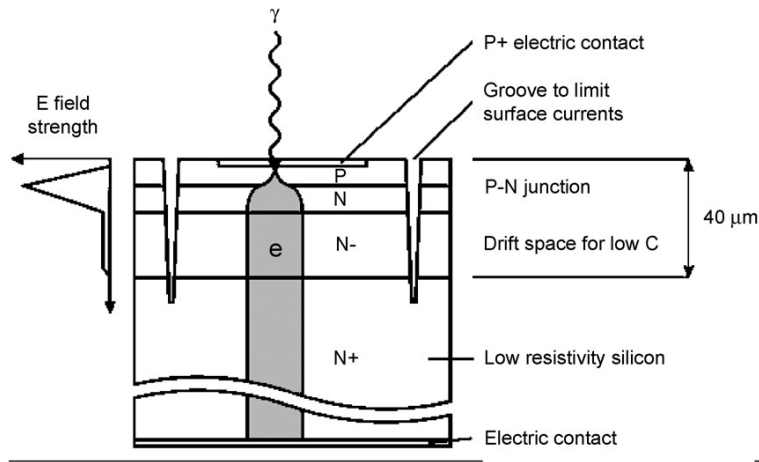
Figure 1: Structure and operation principle of an APD. The design of a G-APD is identical. Picture taken from [1].

1.3 Diode characteristics

1.3.1 Photon detection efficiency

The total probability that a single photon arriving at the diode surface initiates a breakdown is called photon detection efficiency (PDE). The PDE is not only dependent on the quantum efficiency, two other factors are important. Due to the division of the diode surface into cells, a part of the diode surface is occupied with conductor paths and thus not photosensitive. A geometry factor ε_{geo} is necessary. The second factor is required since not all electron-hole pairs initiate a breakdown. The breakdown probability ε_{bd} is voltage dependent up to the state where every electron-hole pair creates an avalanche. The PDE is the product $PDE = \varepsilon_{geo} \cdot QE \cdot \varepsilon_{bd}$.

1.3.2 Gain

In Geiger-mode the total charge released per cell is linear in the difference between bias voltage and breakdown voltage. The linear coefficient is the capacitance C_c of the cell, the gain M is given by $M = \frac{C_c}{e}(V_b - V_{br})$ where e is the elementary charge. The gain of a G-APD is typically in the range of $10^5 - 10^7$.[1] The breakdown voltage is temperature dependent. Electron propagation in the semiconductor is impeded by lattice vibrations (phonons). This increases the necessary voltage to achieve breakdown at higher temperatures. If the bias voltage stays constant, a higher temperature leads to a lower gain. The temperature dependence of the breakdown voltage is studied in chapter 2.2.

1.3.3 Saturation

The distribution of the incoming photons on the cells is a statistical process. If multiple photons hit the same cell and create independent electron-hole pairs, the output signal is identical to the case where only one photon initiates the avalanche.

If every incoming photon hit a different cell, the number of triggered cells would be given by $N_0 = N_{inc} \cdot PDE$. Due to the random distribution of the photons on the cells where several photons may hit the same cell, the number of triggered cells is statistically reduced to $N_0 = N_c(1 - e^{-\frac{N_{inc} \cdot PDE}{N_c}})$[2]. N_c is the number of cells. For later calculations a saturation function S is defined as $S(N_{pe}, N_c) := N_c(1 - e^{-\frac{N_{pe}}{N_c}})$.

1.3.4 Crosstalk

During the breakdown, a plasma with a very high temperature forms which excites electrons to high energy levels. The photons emitted when these electrons relaxate can trigger neighboring cells, increasing the number of triggered cells. The crosstalk probability p_{ct} is defined as the probability that a triggered cell triggers one or more other cells through crosstalk. Note that p_{ct} is not the probability to trigger *one* cell through crosstalk. The used definition is a well-measurable quantity (see section 2.3).

The mean number μ_{ct} of triggered cells per initially triggered cell is not identical to the crosstalk probability p_{ct}. Assuming a Poisson distributed number of crosstalk cells per initial cell, μ_{ct} is given by $\mu_{ct} = -ln(1 - p_{ct})$. In a linear approximation, μ_{ct} is equal to p_{ct}.

Since the number of emitted photons per breakdown is dependent on the extent of the avalanche, the crosstalk probability p_{ct} depends on the gain and therefore on the bias voltage and temperature.

1.3.5 Afterpulses

During breakdown, electrons may be trapped e.g. in crystal defects. The delayed release of trapped electrons occurs with exponentially decreasing probability. The afterpulse rate is a time-dependent function. When diode pulses are integrated, the number of included afterpulses depends on the integration time t_{int}. The mean number of afterpulses during a certain integration time after a primary breakdown is called afterpulse probability p_{ap}. This definition includes the increased probability for a second afterpulse after a first one occurred.

After a breakdown a cell needs some time until a new breakdown reaches the same level. Afterpulses occurring during this recovery time do not contribute the charge of a full breakdown to the signal. In analogy to the crosstalk a mean value μ_{ap} is defined, which is the equivalent mean number of full breakdowns to be added due to afterpulses to each cell with a breakdown. Note that this definition includes the crosstalk of the afterpulses. μ_{ap} also includes the loss of charge when an afterpulse occurs shortly before the integration gate ends. The measurement of the afterpulse probability and the necessary calculations are described in section 2.4.

The release of the trapped electrons occurs via phonons. The amount of available phonons is temperature dependent, thus the time constant of the exponential function is temperature dependent. The number of trapped electrons increases with larger gain, which makes afterpulses dependent on the bias voltage.

1.3.6 Dark count

Besides the generation through incoming photons, crosstalk and afterpulses, electron-hole pairs can be generated through thermal effects and tunneling[1, 3] and initiate a cell breakdown independently of incoming photons. The dark count rate R_{dc} is the number of breakdowns occurring per unit time when no light arrives on the diode surface. The afterpulses of an initial dark count event are counted as distinct events. Events with more than one triggered cell due to crosstalk are counted as one event.

The dark count rate is usually measured by applying a threshold to the diode signal which is half of the signal size that occurs for a single triggered cell (sometimes referred to as "0.5thr"). The rate of events above this threshold is measured. This threshold cuts away afterpulses occurring when the cell is recovered less than 50 %. If the threshold is set to 1.5 cells only dark count events which trigger at least one more cell through crosstalk are counted.

For PET applications, dark count is usually neglected. The dark count rate is typically some megahertz. Even for a long integration time of a few hundred nanoseconds dark count amounts to less than one dark count event. This is negligible compared to the expected signals of a hundred to more than a thousand triggered cells.

1.4 Calculation of the mean number of breakdowns

1.4.1 General case

In this section, the mean number of breakdowns of a G-APD during a certain time window is calculated when N_{inc} photons arrive at the surface of the diode. The mean number of breakdowns depends on the number of incoming photons, the photon detection efficiency (PDE), the influence of saturation, crosstalk and afterpulses and some amount of cells triggered by dark count. The calculation is as follows:

- The number of photons hitting the diode surface is N_{inc}.

- The number of photons triggering an avalanche is $N_{pe} = PDE \times N_{inc}$. N_{pe} is referred to as "number of detected photons". N_{pe} is sometimes called "number of photoelectrons", which is slightly misleading due to the fact that crosstalk cells are also triggered by optical photons. Nonetheless the index "pe" is used for consistency.

- Taking saturation into account the initial number of triggered cells is $N_0 = S(N_{pe}, N_c)$.

- The mean number of cells triggered by crosstalk is per definition $\mu_{ct} \cdot N_0$ without saturation. Two saturation processes are relevant: first a fraction of the crosstalk photons hit one of the N_0 cells which were already triggered and thus insensitive. The probability of this primary crosstalk saturation process is $\frac{N_0}{N_c}$ and reduces the number of crosstalk cells to $\frac{N_c - N_0}{N_c} \cdot \mu_{ct} \cdot N_0$. The second saturation process is the self-saturation of the crosstalk cells: the number of available cells is $N_c - N_0$, therefore the number of cells triggered by crosstalk is $N_{ct} = S(\frac{N_c - N_0}{N_c} \cdot \mu_{ct} \cdot N_0, N_c - N_0)$.

- The equivalent number of full breakdowns to be added due to afterpulses is $N_{ap} = \mu_{ap}(N_0 + N_{ct})$.

- The mean number of dark count events is given by $N_{dc} = R_{dc} \times t_{int}$ without saturation, where R_{dc} is the dark count rate and t_{int} the integration time.

- The total number of breakdowns during the time t_{int} is $\tilde{N} = N_0 + N_{ct} + N_{ap} + N_{dc}$.

$\tilde{N}$ can be rewritten using the terms from above:

$$\tilde{N} = N_0 + \underbrace{S\left(\frac{N_c - N_0}{N_c} \cdot \mu_{ct} \cdot N_0, N_c - N_0\right)}_{N_{ct}} + \underbrace{\mu_{ap}(N_0 + N_{ct})}_{N_{ap}} + N_{dc} \quad (1.1)$$

$$N_0 = S(N_{pe}, N_c) = N_c(1 - e^{-\frac{N_{pe}}{N_c}}) \quad (1.2)$$

1.4.2 Approximation for AX-PET

Besides neglecting the dark counts (see section 1.3.6), it has to be questioned whether the self-saturation of the crosstalk has to be taken into account. The number of photons which trigger an avalanche N_{pe} is expected between 1000 and 1500 for the larger signals from the crystals. A simple calculation will show if it is necessary to include self-saturation for the calculation of the number of cells triggered by crosstalk. The upper limit of the expected range is taken where the effect is largest. The initial number of triggered cells is $N_0 = S(1500, 3600) = 1227$. Assuming $\mu_{ct} = 10\%$ crosstalk (see section 2.3), the number of cells triggered through crosstalk is 123 without saturation. Primary crosstalk saturation reduces this number to 81. Including self-saturation, the number of crosstalk cells is $N_{ct} = 79$. The difference of 2 is negligible compared to the sum $N_0 + N_{ct} = 1306$.
Equation (1.1) is reduced to

$$\tilde{N} = N_0 + \underbrace{\frac{N_c - N_0}{N_c} \cdot \mu_{ct} \cdot N_0}_{N_{ct}} + \underbrace{\mu_{ap}(N_0 + N_{ct})}_{N_{ap}}$$

$$= N_0\left(1 + \frac{N_c - N_0}{N_c}\mu_{ct}\right)(1 + \mu_{ap}) \quad (1.3)$$

$$N_0 = S(N_{pe}, N_c) = N_c(1 - e^{-\frac{N_{pe}}{N_c}}) \quad (1.4)$$

The smaller signals from the WLS strips are expected to consist of less than 150 detected photons. In this case, the primary saturation of crosstalk and the saturation of N_{pe} are neglected too:

$$\tilde{N} = N_0(1 + \mu_{ct})(1 + \mu_{ap}) \quad (1.5)$$

$$N_0 = N_{pe} \quad (1.6)$$
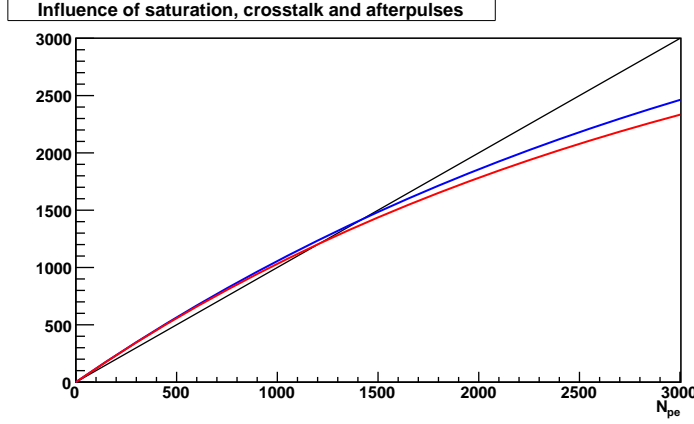
Figure 2: Number of breakdowns depending on the number of detected photons N_{pe} for a diode with $N_c = 3600$ cells. The plot shows N_{pe} (black), the calculated number of breakdowns including all effects (red) and the number of breakdowns when neglecting primary saturation and self-saturation of crosstalk (blue). For crosstalk and afterpulses the values $\mu_{ct} = 0.1$ and $\mu_{ap} = 0.1$ are used. If N_{pe} is small (i.e. smaller than 200), both crosstalk saturation effects can be neglected. The number of breakdowns can be larger than the number of cells due to afterpulses.

1.5 Calculation of the number of detected photons from a measured number of breakdowns

The calculation from the last chapter calculates the number of breakdowns when the number of incoming photons is known. For a measurement, the inverse calculation is of interest: a certain number of breakdowns $\tilde{N} \pm \Delta\tilde{N}$ is measured, and the number of detected photons $N_{pe} \pm \Delta N_{pe}$ has to be calculated.

This calculation cannot be done analytically for the general case. The approximation which neglects dark counts and the self-saturation of crosstalk (equations (1.3) and (1.4)) can be solved. First the number of initial breakdowns N_0 is calculated from the number of measured breakdowns $\tilde{N}$. Then the number of detected photons N_{pe} is calculated from the number of initial breakdowns.

Equation (1.3) is a quadratic equation in N_0 with two solutions. According to equation (1.4), N_0 has to be smaller than N_c which defines the correct one.

$$
\begin{aligned}
N_0 &= \frac{1}{2\mu_{ct}} \left[N_c(1 + \mu_{ct}) \pm \sqrt{N_c^2(1 + \mu_{ct})^2 - \frac{4\mu_{ct}N_c\tilde{N}}{1 + \mu_{ap}}} \right] \\
&\overset{(1.4)}{=} \frac{1}{2\mu_{ct}} \left[N_c(1 + \mu_{ct}) - \sqrt{N_c^2(1 + \mu_{ct})^2 - \frac{4\mu_{ct}N_c\tilde{N}}{1 + \mu_{ap}}} \right] \quad (1.7)
\end{aligned}
$$

$$
N_{pe} = N_c \cdot ln\left(\frac{N_c}{N_c - N_0} \right) \quad (1.8)
$$

The result for N_0 can be checked by developing the square root in a Taylor

7

polynomial of first order. N_0 simplifies to

$$N_0 \approx \frac{\tilde{N}}{(1 + \mu_{ct})(1 + \mu_{ap})},$$

which is identical to the result when not only the self-saturation of crosstalk but also its primary saturation is neglected ($\frac{N_c - N_0}{N_c}$ in equation (1.3)).
The calculation of ΔN_{pe} is more complicated:

$$\Delta N_0 = \sqrt{\left(\frac{dN_0}{d\tilde{N}}\Delta\tilde{N}\right)^2 + \left(\frac{dN_0}{d\mu_{ct}}\Delta\mu_{ct}\right)^2 + \left(\frac{dN_0}{d\mu_{ap}}\Delta\mu_{ap}\right)^2} \quad (1.9)$$

$$\Delta N_{pe} = \Delta N_0 \frac{N_c}{N_c - N_0} \quad (1.10)$$

where

$$\frac{dN_0}{d\tilde{N}} = \frac{N_c}{D(1 + \mu_{ap})}$$

$$\frac{dN_0}{d\mu_{ct}} = -\frac{N_0}{\mu_{ct}} + \frac{1}{2\mu_{ct}}\left(N_c - \frac{1}{2D}(2N_c^2(1 + \mu_{ct}) - \frac{4N_c\tilde{N}}{1 + \mu_{ap}})\right)$$

$$\frac{dN_0}{d\mu_{ap}} = -\frac{N_c\tilde{N}}{D(1 + \mu_{ap})^2}$$

$$D := \sqrt{N_c^2(1 + \mu_{ct})^2 - \frac{4\mu_{ct}N_c\tilde{N}}{1 + \mu_{ap}}}.$$

If the primary saturation of the crosstalk is neglected, ΔN_0 can be simplified:

$$\Delta N_0 = N_0 \sqrt{\left(\frac{\Delta\tilde{N}}{\tilde{N}}\right)^2 + \left(\frac{\Delta\mu_{ct}}{1 + \mu_{ct}}\right)^2 + \left(\frac{\Delta\mu_{ap}}{1 + \mu_{ap}}\right)^2} \quad (1.11)$$

The number of initial photons is calculated using the equations (1.7) and (1.8). To estimate the error of the calculation, equation (1.10) and one of the equations (1.9) or (1.11) has to be used. In this paper, the simplified equation (1.11) is used.

1.6 Calculation of the excess noise factor (ENF)

The excess noise factor (ENF) quantifies the deviation of the energy resolution from the statistical variation of the number of detected photons $N_\gamma \cdot PDE$. It is given by the equation

$$\frac{\sigma}{E} = \sqrt{\frac{ENF}{N_\gamma \cdot PDE}} \quad (1.12)$$

when readout noise is neglected. For G-APDs the main contributions to the ENF are the variation in the released charge per breakdown and the variations of saturation, crosstalk and afterpulses (i.e. the number of breakdowns). For

this calculation, the charge variation is neglected. Using the terminology of the previous chapter, the equation above becomes

$$\begin{aligned} \frac{\sigma_{\tilde{N}}}{\tilde{N}} &= \sqrt{\frac{ENF}{N_{inc}PDE}} \\ &= \sqrt{\frac{ENF}{N_{pe}}} \end{aligned} \tag{1.13}$$

The case where dark counts and self-saturation of crosstalk are neglected is studied (equation (1.3)). An approximation is made for the primary saturation. An effective crosstalk correction is defined: $\hat{\mu}_{ct} := \frac{N_c - N_0}{N_c}\mu_{ct}$. For the calculation, $\hat{\mu}_{ct}$ is treated as being independent of N_0. This approximation neglects the dependency of $\hat{\mu}_{ct}$ on N_0 in the range $N_0 \pm \sigma_{N_0}$.

The ENF is found by calculating $\sigma_{\tilde{N}}$, which depends on the statistical variations of the occurring processes:

- The standard deviation of the number of initial breakdowns N_0 be σ_{N_0} for now, two cases are considered later.

- The standard deviation of the number of cells triggered by crosstalk $N_{ct} = \hat{\mu}_{ct} \cdot N_0$ is split into two components: the first component is $\sigma_{ct,indep} = \sqrt{N_{ct}} = \sqrt{\hat{\mu}_{ct}N_0}$, the Poisson error of the number of crosstalk cells. The second error is the inherited error from N_0 and is $\sigma_{ct,dep} = \hat{\mu}_{ct}\sigma_{N_0}$. This value is correlated to the standard deviation of N_0 and has therefore to be added linearly.

- As for the crosstalk, the standard deviation of the afterpulses is split into two components. The dependent error is $\sigma_{ap,dep} = \mu_{ap}\sigma_{N_0+N_{ct}}$. The independent part is approximated by $\sigma_{ap,indep} = \sqrt{N_{ap}} = \sqrt{\mu_{ap}N_0(1 + \hat{\mu}_{ct})}$. This is only an approximation since μ_{ap} is the equivalent number of full breakdowns. The correct value is the recovery-time weighted integral of the standard deviation of the number of afterpulses per time.

First the standard deviation $\sigma_{N_0+N_{ct}}$ of the sum of N_0 and the crosstalk events N_{ct} is calculated:

$$\begin{aligned} \sigma_{N_0+N_{ct}} &= \sqrt{(\sigma_{N_0} + \sigma_{ct,dep})^2 + \sigma_{ct,indep}^2} \\ &= \sqrt{(\sigma_{N_0}(1 + \hat{\mu}_{ct}))^2 + \hat{\mu}_{ct}N_0} \\ &= \sqrt{\sigma_{N_0}^2(1 + \hat{\mu}_{ct})^2 + \hat{\mu}_{ct}N_0} \end{aligned} \tag{1.14}$$

Using this result the standard deviation of $\tilde{N}$ is

$$\begin{aligned} \sigma_{\tilde{N}} &= \sqrt{(\sigma_{N_0+N_{ct}} + \sigma_{ap,dep})^2 + \sigma_{ap,indep}^2} \\ &= \sqrt{\sigma_{N_0+N_{ct}}^2(1 + \mu_{ap})^2 + \mu_{ap}(1 + \hat{\mu}_{ct})N_0} \\ &= \sqrt{(\sigma_{N_0}^2(1 + \hat{\mu}_{ct})^2 + \hat{\mu}_{ct}N_0)(1 + \mu_{ap})^2 + \mu_{ap}(1 + \hat{\mu}_{ct})N_0}. \end{aligned} \tag{1.15}$$

Combining equation (1.15) and (1.3) the energy resolution is

$$
\begin{aligned}
\frac{\sigma_{\tilde{N}}}{\tilde{N}} &= \frac{\sigma_{\tilde{N}}}{N_0(1+\hat{\mu}_{ct})(1+\mu_{ap})} \\
&= \sqrt{\frac{1}{N_0}\left(\frac{\sigma_{N_0}^2}{N_0} + \frac{\hat{\mu}_{ct}}{(1+\hat{\mu}_{ct})^2} + \frac{\mu_{ap}}{(1+\mu_{ap})^2(1+\hat{\mu}_{ct})}\right)}. \quad (1.16)
\end{aligned}
$$

As a first example saturation is neglected ($N_0 = N_{pe}$). This is valid for small numbers of detected photons N_{pe}, and the primary saturation of the crosstalk can be neglected too: $\hat{\mu}_{ct} = \mu_{ct}$. N_{pe} is a Poisson variable, therefore $\sigma_{N_0} = \sqrt{N_0}$, and the energy resolution can be written as

$$
\frac{\sigma_{\tilde{N}}}{\tilde{N}} = \sqrt{\underbrace{\frac{1}{N_0}}_{1/N_{pe}}\underbrace{\left[1 + \frac{\mu_{ct}}{(1+\mu_{ct})^2} + \frac{\mu_{ap}}{(1+\mu_{ap})^2(1+\mu_{ct})}\right]}_{ENF}}. \quad (1.17)
$$

If saturation is taken into account, then the standard deviation of N_0 has a contribution from N_{pe} through standard error propagation plus a contribution from the variation of the number of lost cells due to saturation. The first contribution is $\sigma_{N_0,dep} = \sigma_{N_{pe}} \cdot \frac{d}{dN_{pe}}S(N_{pe},N_c) = \sigma_{N_{pe}}e^{-\frac{N_{pe}}{N_c}}$. The second contribution assumes a Poisson distributed number of lost cells: $\sigma_{N_0,indep} = \sqrt{N_{pe}-N_0}$.

$$
\begin{aligned}
\sigma_{N_0} &= \sqrt{\sigma_{N_0,dep}^2 + \sigma_{N_0,indep}^2} \\
&= \sqrt{(\sigma_{N_{pe}}e^{-\frac{N_{pe}}{N_c}})^2 + \sqrt{N_{pe}-N_0}^2} \\
&= \sqrt{N_{pe}(1 + e^{\frac{-2N_{pe}}{N_c}}) - N_0} \quad (1.18) \\
\frac{\sigma_{\tilde{N}}}{\tilde{N}} &= \sqrt{\frac{1}{N_0}\left(\frac{N_{pe}(1+e^{\frac{-2N_{pe}}{N_c}})}{N_0} - 1 + \frac{\hat{\mu}_{ct}}{(1+\hat{\mu}_{ct})^2} + \frac{\mu_{ap}}{(1+\mu_{ap})^2(1+\hat{\mu}_{ct})}\right)}
\end{aligned}
$$
$$(1.19)$$
$$
\begin{aligned}
\hat{\mu}_{ct} &= \frac{N_c - N_0}{N_c}\mu_{ct} \\
N_0 &= N_c(1 - e^{\frac{-N_{pe}}{N_c}})
\end{aligned}
$$

The excess noise factor is the square of the energy resolution multiplied by N_{pe}:

$$
ENF = N_{pe}\left(\frac{\sigma_{\tilde{N}}}{\tilde{N}}\right)^2
$$

1.7 Parameter dependencies

The parameters used to calculate the number of breakdowns for a certain number of photons impinging on the diode depend on each other and some external conditions. The following list gives an overview of these dependencies. Not listed are dependencies on the type of the diode such as the influence of the cell number on the saturation or the geometric factor ε_{geo} in the PDE.

Breakdown voltage V_{br}: The breakdown voltage is temperature dependent: $V_{br}(T)$

Quantum efficiency QE: The quantum efficiency depends on the wavelength of the incoming photons: $QE(\lambda)$

Avalanche probability ε_{bd}: The avalanche probability depends on the difference between bias and breakdown voltage and on the wavelength of the incoming photon: $\varepsilon_{bd}(\lambda, V_b - V_{br}(T))$

Photon detection efficiency PDE: The photon detection efficiency adopts the dependencies of its factors: $PDE(QE(\lambda), \varepsilon_{bd}(\lambda, V_b - V_{br}(T)))$

Gain M: The gain depends on the difference between bias and breakdown voltage: $M(V_b - V_{br}(T))$

Crosstalk probability p_{ct}: The crosstalk probability depends on the size of the avalanche, which is equivalent to the gain: $p_{ct}(M(V_b - V_{br}(T)))$

Afterpulse probability p_{ap}: p_{ap} depends on the temperature, gain and the integration time: $p_{ap}(T, M(V_b - V_{br}(T)), t_{int})$

Dark count rate R_{dc}: The dark count rate depends on the temperature and the voltage difference: $R_{dc}(T, V_b - V_{br}(T))$

2   Characterisation of G-APDs

2.1   Experimental setup

The properties described in the previous chapter vary for diodes of different manufacturers. All measurements in this chapter were made with the same diode from Hamamatsu Photonics[1]. G-APDs from Hamamatsu are called Multi-Pixel Photon Counters (MPPCs). The used device has a size of $3 \times 3 \, \mathrm{mm}^2$, each of the 3600 cells (pixels) has a size of $50 \times 50 \, \mu\mathrm{m}^2$. The proposed bias voltage at room temperature ($25 \, ^\circ\mathrm{C}$) is $V_b = 69.6 \, \mathrm{V}$, yielding a gain of $M = 5.77 \cdot 10^5$. For the measurements, the diodes are installed on a low noise amplifier and placed in a metal box to reduce temperature variations and electromagnetic pickup noise. Bias voltage is supplied by a Keithley 487 picoammeter voltage source. The number of breakdowns at the same time is small, the mean value is below ten for all measurements. Therefore saturation is neglected. For such small signals, electronic noise is a problem. The absolute released charge is not important for the measurements, only the distinction of the different numbers of breakdowns. Signals are amplified and shaped with an ORTEC Timing Filter Amplifier. To achieve the necessary low noise level, integration gates are kept short (10 ns or less).

The signals are integrated using either a standard LeCroy ADC 2249A or the integration function of a LeCroy WaveRunner 64Xi oscilloscope. The integration gate for the ADC is generated by discriminating the splitted signal in a SIN Constant Fraction Discriminator (CFD) whose output gate is used as the input of a LRS 821 Quad Discriminator. The second discriminator is necessary since the length of the gate produced by the CFD is not stable.

For the oscilloscope measurements, the ADC gate is used as a trigger to ensure the same selection of pulses for the scope and ADC measurements. The integration gate is a scope setting, allowing very short and precise gates. Due to this advantage over the measurements with the LeCroy 2249A, all measurements presented in this paper are made with the oscilloscope. A typical oscilloscope screen with the discriminator gate used as trigger, MPPC signal after shaping and scope integration gate is shown in figure 3.

For measurements using a pulsed light source, the clock generator of the light source is used instead of the discriminated diode signal to determine the gate. For weak light pulses, the diode signal during the integration gate contains zero, one or more breakdowns. In the spectrum obtained by integrating the signals, the peaks relate to the different numbers of breakdowns (figure 4).

All data analysis is performed using the standard MINUIT fit algorithm in the ROOT[2] analysis framework.

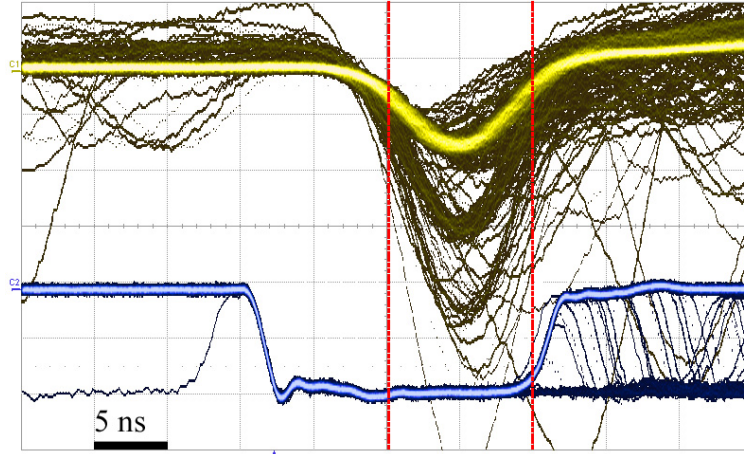## 2.2   Temperature dependence of the breakdown voltage

2.2.1   Method

The gain of a G-APD is linear in the difference between bias and breakdown voltage. Therefore the breakdown voltage can be found by fitting a straight line to the gain at different voltages. A weak light pulse is guided onto the MPPC
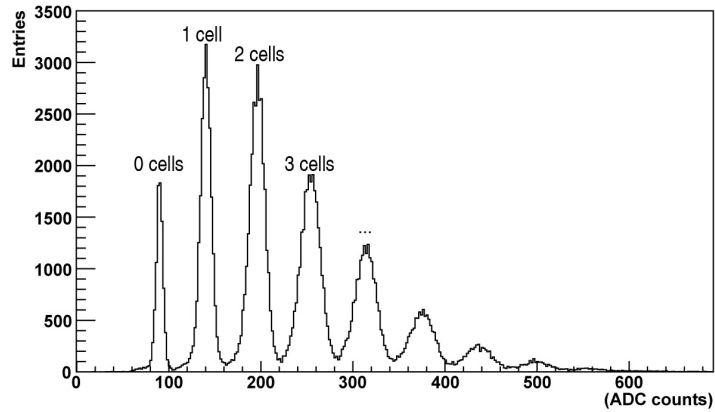
---

[1]http://www.hamamatsu.com/
[2]http://root.cern.ch/

Figure 3: Typical screen of the oscilloscope with the discriminator gate (blue) and the amplified and shaped MPPC signal (yellow). The vertical lines (red) indicate the integration gate used by the oscilloscope. Three signal sizes can be distinguished, relating to one, two and three breakdowns.

Figure 4: Typical spectrum obtained using a pulsed LED shining on the diode. The LED clock is used as a trigger signal for the oscilloscope, where the diode signal is integrated during 10 ns. The peaks relate to 0, 1, 2 and more breakdowns, the number of events per peak are basically Poisson distributed (see section 2.3.3 for details).

13

with a glass fibre, triggering a small number of cells (Poisson mean $\mu = 2.2$). The peaks in the ADC spectrum are fitted with gaussian curves and the position difference extracted. These values are proportional to the gain. The absolute gain cannot be calculated using the ADC to charge conversion factor since only part of the signal is integrated.

The peak differences are measured for a set of bias voltages at the three temperatures $5\,°C$, $15\,°C$ and $25\,°C$. The peak differences are plotted against the bias voltage and a linear fit applied. The extrapolation to gain 0 reveals the breakdown voltage.

2.2.2   Results

Figure 5 on the following page shows the plots for the three measurements. The square of the correlation coefficient is above 0.998 for all fits. The resulting breakdown voltages are $67.49\,V$, $68.04\,V$ and $68.53\,V$ for $5\,°C$, $15\,°C$ and $25\,°C$, respectively. The breakdown voltages are known with a precision of 0.01 V, the temperature with a precision of $0.5\,°C$. A linear fit (figure 6) yields a change of $52 \pm 1\,mV$ per $°C$.

2.2.3   Discussion

The observed characteristics of the breakdown voltage is close to the value provided by Hamamatsu[2], which is $55\pm1\,mV$ per $°C$ for a chip size of $1\times1\,mm^2$. A dependence on the chip size is not assumed since the relevant process is confined to one cell.

The correlation coefficent close to 1 confirms the linearity of the gain in the bias voltage.

2.3   Crosstalk measurements

To measure the amount of crosstalk, two methods are evaluated. The first method uses dark count events. Dark count events trigger initially only one cell, sometimes additional cells are triggered through crosstalk. This approach is called "dark count method" throughout this paper. The second method called "Poisson method" uses a weak light pulse, where the number of photons detected by the diode is Poisson distributed. Crosstalk redistributes some events in the peak spectrum. The difference between the expected and the observed spectrum is used to calculate the crosstalk probability.

2.3.1   The dark count method

The threshold in the CFD is set to 0.5 cells. The peak region of the signals is integrated. The spectrum shows peaks relating to events with one and two breakdowns. A threshold between the two peaks is set and the events above threshold counted. These are events where a second or more cells were triggered due to crosstalk. The ratio (events above threshold)/(total number of events) is the crosstalk probability. An alternative method is to fit Gaussian peaks into the spectra, thus neglecting events between the peaks. Such events can be explained due to the fact that some events are located on the tail of earlier events. Since the used shaping causes "overshooting", a shift to lower ADC values is also possible.
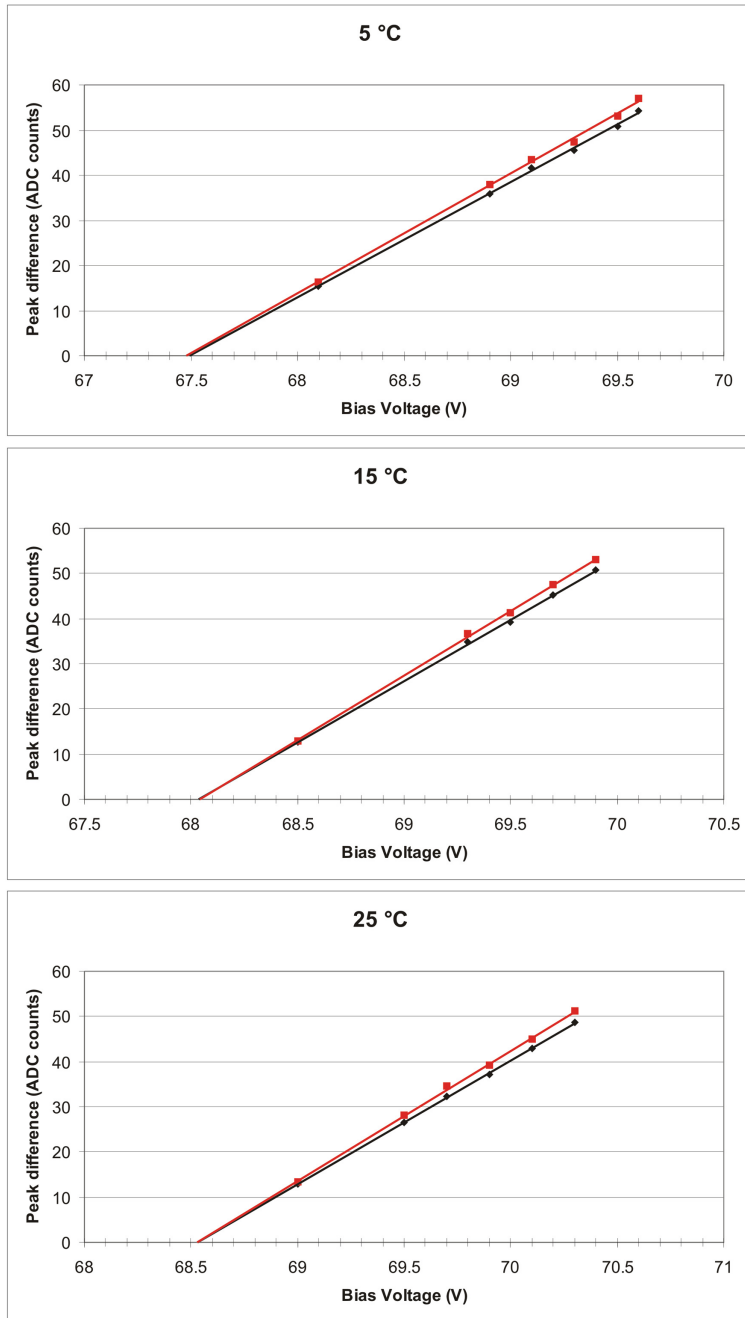
Figure 5: Gain vs. bias voltage at three different temperatures with linear fit curves. The y-coordinate is proportional to the gain. The black curve is the difference between the two cells and the one cell signal peaks, the red curve between the three cells and the two cells signal peaks. The mean value of the two zero crossings is used.

15
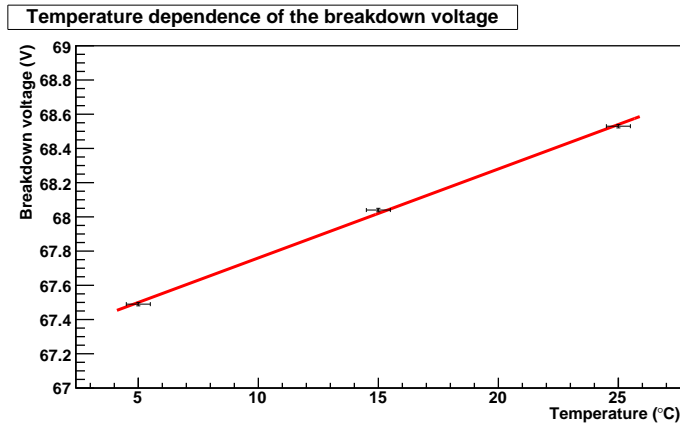
Figure 6: Change of the breakdown voltage with ambient temperature. The breakdown voltage rises linearly with $52 \pm 1\,\text{mV}$ per $^\circ\text{C}$.

Afterpulses are neglected in the analysis since the gate length was kept very short ($10\,\text{ns}$). Combined with the recovery time of the cells of $50\,\text{ns}$[4], afterpulses cannot contribute the same charge as a cell triggered by crosstalk. Thus afterpulses do not change the distribution of events onto the peaks, the obtained result is independent of afterpulses.

The precision of the obtained result is estimated by varying the threshold.

2.3.2 Dark count method: Comparison between threshold cut and Gaussian fit

The dark count method simply compares the number of events in the peaks corresponding to more than one breakdown with the total number of events. For the classification of events to a peak, two methods were tested: the first one sets a threshold between the peaks, all events above threshold are counted as crosstalk events, and the crosstalk probability is given by $p_{ct} = N_{aboveThr}/N_{tot}$. Since the level of events between the two peaks is not zero, events from the overlap region are assigned to the wrong peak. It is assumed that the number of wrongly assigned events is approximately the same in both directions. An error estimate is found by varying the threshold.

The second method uses Gaussian fits for the peaks. The area under the peaks is calculated. The crosstalk probability is given by the sum of the areas of the peaks for two and more cells divided by the sum of all peaks. The error of this method is difficult to specify. The errors of the fit are negligible compared to the amount of events that are "cut off" because they are outside the peaks. Including these events is the same as going back to the threshold method. Another problem is that peaks with more than two cells cannot be fitted since the amount of events collected during the measurements is not large enough. Neglecting those peaks results in a systematic error.

Because the threshold method allows to specify an error range and needs no correction of systematic errors, that method is used for all measurements.

16

2.3.3 The Poisson method

If a pulsed light shining on a G-APD is very weak, only a few cells per light pulse are triggered. For this measurement, the ADC gate is not generated by discriminating the MPPC signal but by using the same clock generator that controls the light source. The light pulse duration has to be short compared to the gate length since differences in the arrival time of the photons widen the histogram peaks.

The number of photons arriving on the chip surface is Poisson distributed:

$$P(n, \mu) = \frac{e^{-\mu} \mu^n}{n!} \tag{2.1}$$

Due to the basic properties of the Poisson distribution, also the number of photons creating an electron-hole pair and the number of cells with a primary breakdown are Poisson distributed, only the mean value being scaled according to the geometric factor, the quantum efficiency and the breakdown probability. The distribution of the events on the peaks in the spectrum is Poissonian ($N_i = N_{tot} \cdot P(i, \mu)$), except that events with one or more breakdowns may trigger additional cells through crosstalk. This leads to a redistribution of events to peaks with higher cell numbers. In particular the peak corresponding to one breakdown gets depopulated.

The peak corresponding to zero breakdowns is unaffected by crosstalk. The Poisson mean can be calculated using the number of events in this peak N_0 and the total number of events N_{tot}:

$$\mu = -ln\left(\frac{N_0}{N_{tot}}\right) \tag{2.2}$$

The expected number of events in the peak corresponding to one breakdown is $N_1 = N_{tot} e^{-\mu} \mu$. The difference between the expected number of events N_1 and the actually measured value $\tilde{N}_1$ is the number of crosstalk events. The crosstalk probability is therefore given by

$$p_{ct} = \frac{\tilde{N}_1 - N_1}{\tilde{N}_1}. \tag{2.3}$$

Again, the precision of the obtained result is estimated by varying the threshold.

2.3.4 Comparison between the dark count method and the Poisson method

As the dark count method, the Poisson method uses thresholds between the peaks to determine the number of events per peak. Due to the non-linear calculation of the crosstalk using the Poisson method, the result is much more dependent on the choice of the threshold if the peaks are not clearly separated. Even for well separated peaks as in figure 4, the error range is large (more than 20 %). For most measurements, the noise level is higher and the peak separation worse. Measurements using the Poisson method were therefore not used in the analysis.

	Bias voltage (V) ±0.01 V	Temperature (°C) ±0.5 °C	Method	Crosstalk probability (%)	Absolute error (%)
A	69.2	5	Dark count	19.3	±0.6
	69.75	15	Dark count	19.4	±0.9
	70.2	25	Dark count	19.4	±0.6
B	69.6	24	Dark count	10.3	±0.4
	69.8	24	Dark count	13	±0.6
	70.0	24	Dark count	17.7	±0.9
C	69.6	25	Dark count	10.3	±0.3
	69.6	25	Dark count	10.2	±0.3
	70.2	25	Dark count	20.7	±0.7
D	69.6	25	Poisson	8.9	-0.8+1.7

Table 1: Overview of all crosstalk measurements. The blocks indicate the measurement series: (A) Temperature dependence (B) Voltage dependence (C) Control measurements (D) Evaluation of the Poisson method

2.3.5 Temperature dependence of crosstalk

To evaluate the temperature dependence of crosstalk, the gain has to be kept constant. Since the gain depends linearly on the difference between the bias voltage and the temperature-dependent breakdown voltage, the bias voltage has to be adjusted at different temperatures. Crosstalk is measured at the same three temperatures where the breakdown voltage was determined (see section 2.2 on page 12). The bias voltage is set 1.7 V above breakdown voltage. A plot of the results is shown in figure 7. The reference measurement at the same voltage and temperature is made using a different setup. The temperature dependence (series A in table 1) is measured inside a cooling box, the reference measurement (series C) in the standard metal box where the other measurements are made. To investigate the temperature dependence of the crosstalk, only the measurement series A is selected to exclude systematic errors due to setup differences.

2.3.6 Voltage dependence of crosstalk

Crosstalk is measured at different bias voltages. From table 1, the measurement series B and C are selected. The crosstalk is plotted against the difference between bias and breakdown voltage. For the breakdown voltage, the results from the measurements presented in chapter 2.2 are used. See figure 8 for a plot of the measurements.

2.3.7 Discussion

Crosstalk was measured at $10.25 \pm 0.3\,\%$ at $25\,°C$ with the bias voltage as proposed by Hamamatsu. According to the measurements, crosstalk is independent of the ambient temperature when the voltage difference between bias and breakdown voltage is constant.
From the measurements at different voltages, it is not possible to establish a parametrisation for the voltage dependence of crosstalk. Further measurements
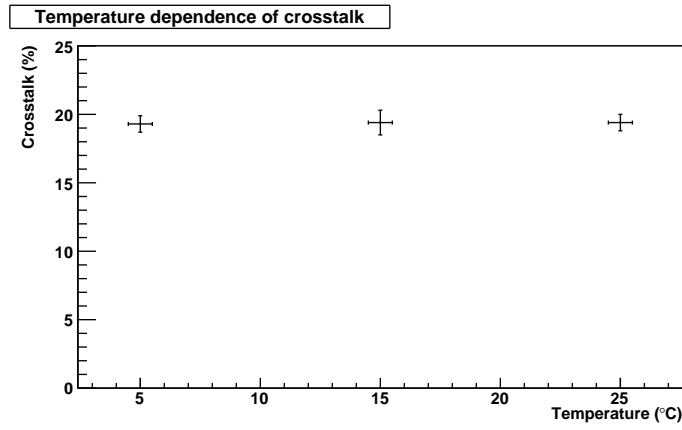
Figure 7: Crosstalk at different temperatures with adjusted bias voltage. The crosstalk is independent of the temperature within the error range.
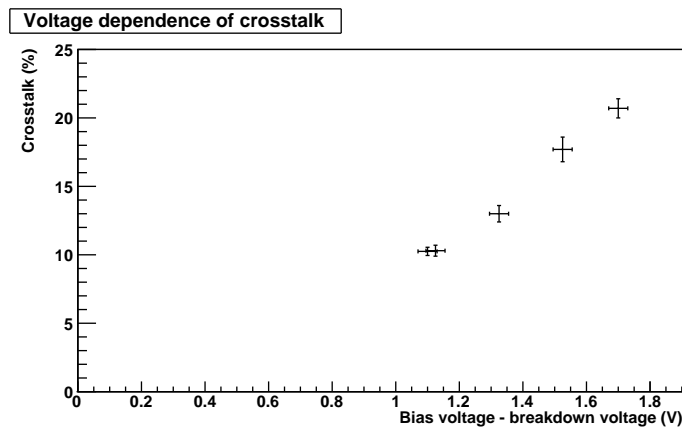
Figure 8: Crosstalk at different bias voltages.

at voltages closer to the breakdown voltage are necessary.

2.4 Afterpulses

To measure the afterpulses, again two different methods were evaluated. The two methods share the basic principle. The discriminated signal from the MPPC is used to open a gate of a certain length. No light shines on the diode, only dark count events occur. During this gate, the number of additional events is counted. This number contains the afterpulses of the initial event and further dark count events. Two parameters can be varied, on the one hand the delay until the gate is opened, on the other hand the length of the gate.

2.4.1 Calculation

The rate of dark count events be g, the rate of afterpulses $f(t - t_0)$. t_0 is the time of the initial event. f is an exponential function with decay time τ and constant N_0/τ. The number of events occurring during the integration gate starting at the time a with gate length $t_{int} = l$ is

$$
\begin{aligned}
N(a,l) &= \int_a^{a+l} [g + f(t - t_0)]\, dt \\
&= \underbrace{g \cdot l}_{darkcounts} + \underbrace{N_0 e^{-\frac{a-t_0}{\tau}}(1 - e^{-\frac{l}{\tau}})}_{afterpulses}.
\end{aligned}
\tag{2.4}
$$

t_0 is set to zero.

For these rate measurements, a correction for the discriminator dead time t_{dt} is necessary. The real number of events during the gate is N, the number of measured events be $\tilde{N}$. The number of missed events is equal to the number of measured events times the mean number of events P that happen during the dead time of the discriminator:

$$
\begin{aligned}
N(a,l) - \tilde{N}(a,l) &= \tilde{N}(a,l) \cdot P \\
N(a,l) &= \tilde{N}(a,l)(1 + P)
\end{aligned}
\tag{2.5}
$$

P is equal to the number of events in the time from t_0 to $t_0 + t_{dt}$:

$$
\begin{aligned}
P &= N(0, t_{dt}) \\
&= \tilde{N}(0, t_{dt})(1 + P) \\
&= \frac{\tilde{N}(0, t_{dt})}{1 - \tilde{N}(0, t_{dt})} \\
1 + P &= \frac{1}{1 - \tilde{N}(0, t_{dt})}
\end{aligned}
\tag{2.6}
$$

P is independent of a and l. Therefore $\tilde{N}(a,l)$ can be measured for different values of the gate delay a and/or the gate length l and the measurement be fitted to obtain $\tilde{g}$, $\tilde{N}_0$ and τ. With those values the correction factor (1+P) can be calculated, the real values are $g = (1 + P)\tilde{g}$ and $N_0 = (1 + P)\tilde{N}_0$. The mean number of afterpulses (i.e. the afterpulse probability) for a gate of length l is $p_{ap} = \int_0^l f(t)dt$.

Due to the recovery time of the diodes (see section 1.3.5), the afterpulses occurring shortly after the initial breakdown release a reduced charge. The recovery function is $r(t - t_0) = 1 - e^{-(t-t_0)/\tau_r}$ with the recovery time $\tau_r = 50\,\text{ns}$[4]. The charge to be added due to afterpulses in units of a full breakdown is $\mu_{ct} = \int_0^l r(t)f(t)dt$. The recovery time has no influence on the measurement since only afterpulse rates are measured and the discriminator threshold is set below the pulse height of a pulse which has recovered only to 26 % (according to the dead time of 15 ns and the recovery time of 50 ns).

2.4.2 Method

The bias voltage of the G-APD is set to 69.6 V. The temperature during the measurement is 25 °C. The diode signal is used as the input of a constant fraction discriminator (CFD). One output of the CFD is led to a delay trigger unit where the measurement gate is created. The other output of the CFD and the output of the delay trigger are led to a coincidence unit (SIN FC104). The second output of the delay trigger and the output of the coincidence unit are led to a scaler where the number of coincidences during one million gates are counted.
The gate length of the CFD was set to 15 ns, thus introducing a well-known dead time to the system which is longer than the dead time of the CFD and the coincidence unit. The dead time of the delay trigger is not relevant.
The two parameters that can be varied are the gate length and the gate delay. Increasing the gate length has the disadvantage that the measured number contains a proportional number of dark count event while the number of afterpulses is not increased. The fitting algorithm is not strong enough to fit data obtained with variable gate length, dividing $N(a, l)$ by l does not improve the performance. Therefore the gate length is kept constant, only the gate delay is varied. The gate length is set to 40 ns, combined with the 15 ns of the CFD gate and the minimal overlap time of the coincidence unit (2 ns) the relevant gate length is 51 ± 2 ns.
For a better fit of the data, the afterpulses are assumed to consist of two components with different decay times.

2.4.3 Results

The plotted data and the fitted curve are found in figure 9. The total afterpulse probability is 21.2 ± 2.0 % per breakdown. The measured dark count rate including its afterpulses is 2.03 ± 0.08 MHz. The first component of the afterpulses has a decay time of 50 ± 6 ns and a total probability of 14.5 ± 1.6 %. The second component has a decay time of 138 ± 22 ns and a total probability of 6.7 ± 1.2 %. Error ranges are obtained by fixing the decay times for the probability errors and vice versa. Since the dark count rate is inverse linear in the gate length, its error bars are deducted from the gate length error.
Using these values, the afterpulse probabilities and the equivalent numbers of full breakdowns μ_{ap} for various gate lengths are listed in table 2.
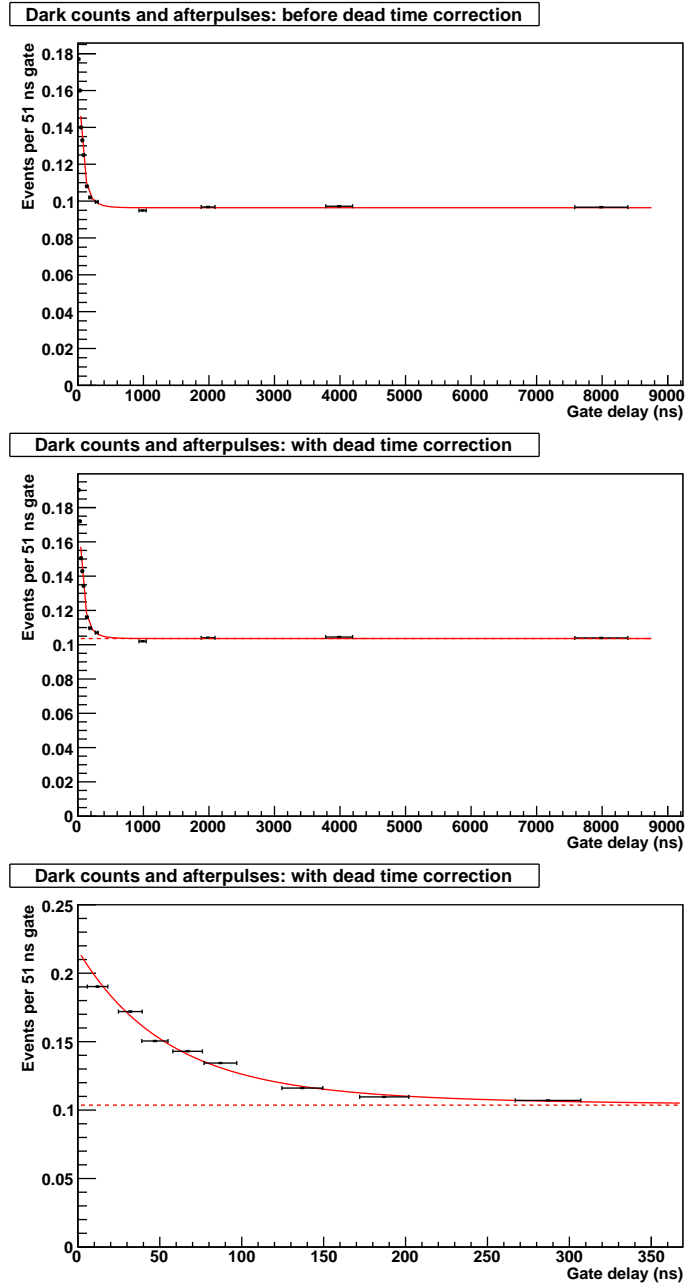
Figure 9: Measurement of afterpulses. Top: data before dead time correction, middle: dead time correction applied, bottom: detail of the corrected plot. The dotted line shows the dark count.

Gate length (ns)	p_{ap} (%)	μ_{ap} (%)
20	5.7	0.94
40	9.6	2.70
51	11.3	3.70
100	16.0	7.21
200	19.3	10.34
inf	21.2	12.17

Table 2: Afterpulse probability (mean number of afterpulses per breakdown) and equivalent number of full breakdowns for various gate lengths.

2.4.4 Discussion

The only reference value for the measurement above is the dark count rate provided by Hamamatsu, for this diode it is 2.052 MHz. The measurements are in very good agreement. The chosen measurement method cannot detect crosstalk. The event opening a gate triggers a mean number of $1 + \mu_{ct}$ cells, thus increasing the number of afterpulses. On the other hand an afterpulse can trigger additional events through crosstalk, but is counted as one event. For the afterpulse probability p_{ap} a correction would be necessary since p_{ap} is defined as the number of afterpulses for one initial cell. The correction factor is $\frac{1}{1+\mu_{ct}}$. However for μ_{ap} the inverse correction factor is necessary to include the crosstalk of the afterpulses. The values provided for p_{ap} are therefore a factor $1 + \mu_{ct}$ too high, the values for μ_{ap} (which are used later) are correct.
The increased probability of a second afterpulse after a first one occurred is already included in the definition of p_{ap} and μ_{ap} and needs no correction.

2.5 Photon detection efficiency

The photon detection efficiency is the product of three factors: the geometry factor, the quantum efficiency and the breakdown probability (see section 1.3.1). The quantum efficiency depends on the wavelength of the incident light, the breakdown probability depends on the bias voltage. In this chapter the dependence on the bias voltage is studied.

2.5.1 Method (voltage dependence of the PDE)

The basic principle used to measure the photon detection efficiency is identical to the Poisson method used to determine crosstalk (see section 2.3.3). But for this measurement, only the Poisson mean number of detected photons is important. The mean number of detected photons is compared to the mean number of a photomultiplier tube (PMT) with known photon detection efficiency. In the G-APD, the Poisson mean is independent of crosstalk and afterpulses since only the zero cell peak is used for the calculation. In comparison with the crosstalk determination, only one threshold has to be set. An error estimate is given by varying the threshold. Dark count events are neglected, their influence is included in the error range when varying the threshold.
The mean number for the photomultiplier tube is calculated by fitting the spectrum with the sum of multiple Gaussian curves. The number of events in the
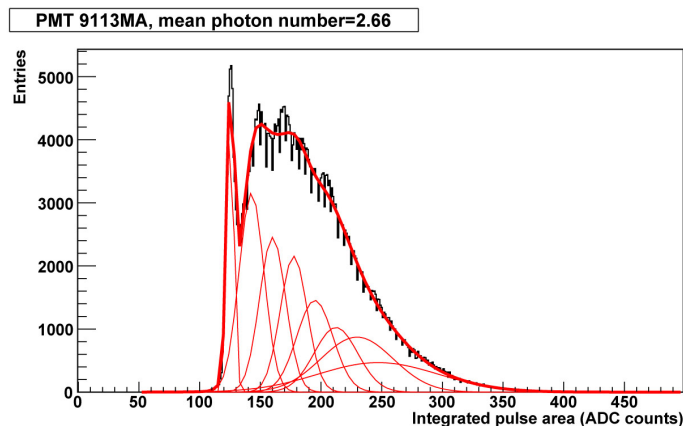
Figure 10: Fit of the calibration measurement with the PMT. The upper peaks being wide does not influence the number of events in the zero peak since their contribution beneath the first Gaussian is negligible.

first peak is given by $N = c\sigma\sqrt{2\pi}$. c and σ are the Gauss constant and standard deviation, respectively.

The LED used is a 450 nm NanoLED by HORIBA Jobin Yvon. The distance between the LED and the G-APD is 343 mm. A first collimator with a diameter of 0.8 mm is installed 12.5 mm from the LED. At a distance of 329 mm, a roughened quartz glass is used to widen the LED beam. A second collimator (diameter 1.0 mm) is placed directly in front of the G-APD/PMT. The LED pulse length is 1 ns. The LED clock generator is used as a trigger for the oscilloscope. The integration gate length is 10 ns. The measurements are conducted at a temperature of 23.5 °C.

First the reference value is measured. A calibrated photomultiplier tube (9113MA by ET Enterprises) is installed with direct contact to the second collimator. At 450 nm, the photomultiplier has a quantum efficiency of 19.06 %, an error of ± 0.1 % is estimated. For the measurements with the G-APD, the alignment of the diode to the collimator was handled with great care, thus ensuring the light beam being centered on the chip with a precision of less than 0.5 mm.

2.5.2 Results (voltage dependence of the PDE)

The number of photons seen by the reference photomultiplier is 2.68 ± 0.02 (see figure 10). This value is the mean value of three measurements. The value obtained for each measurement is within the error range independent of the fit parameters used.

The mean values for the G-APD are listed in table 3. The error values are obtained by varying the threshold. The photon detection efficiency is calculated by dividing the number of detected photons by the reference value and multiplying with the quantum efficiency of the PMT. Figure 11 shows the plotted data. The maximal measured photon detection efficiency is at 70.2 V and is $(39.5 + 0.6 - 1.2)$ %.

Voltage (V)	Mean photon number	+	-	PDE (%)	+ (%)	- (%)
68.7	1.29	0.02	0.03	9.2	0.2	0.3
68.8	1.78	0.01	0.02	12.7	0.2	0.2
69.0	2.63	0.01	0.03	18.7	0.2	0.3
69.3	3.68	0.01	0.03	26.2	0.3	0.4
69.6	4.53	0.02	0.04	32.2	0.4	0.5
69.9	5.12	0.05	0.08	36.4	0.5	0.7
70.2	5.56	0.06	0.15	39.5	0.6	1.2
70.4	5.37	0.14	0.13	38.2	1.4	1.0

Table 3: Results of the measurement of the photon detection efficiency. The error bars are asymmetric, "+" and "-" indicating the direction of the error.
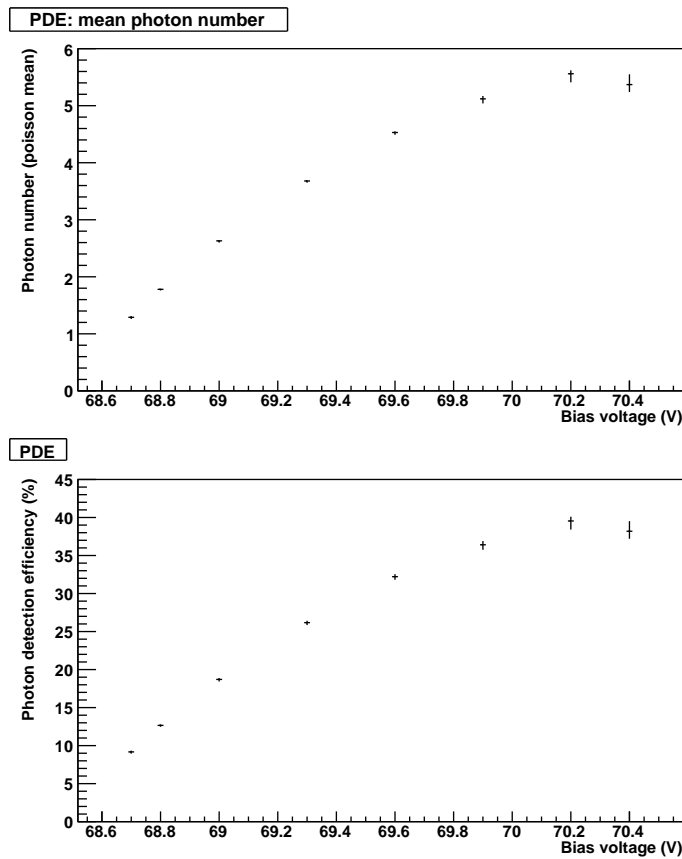
Figure 11: Mean photon number (top) and photon detection efficiency (bottom) at different voltages.

2.5.3 Discussion

The characteristic of the measured data complies with the expectation. The PDE rises for increasing voltage and reaches a maximum when the breakdown probability is 1. The maximum value is lower than the value provided by Hamamatsu for at 450 nm, which is 48 %[2]. While their measurement "includes effects of crosstalk and afterpulses", the method used in this measurement is free of such influences. Correcting their value with $\mu_{ct} = 10.9$ % crosstalk and $\mu_{ap} = 10.34$ % afterpulses (assuming a gate length of 200 ns), their value reduces to 39.2 % in agreement with our measurement.

3 Axial Positron Emission Tomography

3.1 Introduction

3.1.1 Medical application of Positron Emission Tomography

Positron Emission Tomography (PET) is a technology used for medical imaging. A molecule is labelled with a positron emitting isotope and introduced into the body. According to its function in the metabolism, the substance is distributed. The measurement of the decay products of the radioactive isotope allows reconstruction of the location of the isotope decays and therefore the distribution of the molecule.[5]

PET allows to investigate a wide range of metabolic processes. Typical processes and the used isotopes are blood flow (^{15}O), glucose metabolism (^{18}F) and protein synthesis (^{11}C).[6] The essential difference from PET to other imaging technologies is the possibility to display metabolic processes and not only the physical structure as with X-ray, computer tomography (CT) or magnetic resonance imaging (MRI).

3.1.2 Basic principle of the Positron Emission Tomography

The radioactive isotopes used for PET are positron emitters. The positron looses its kinetic energy in collisions and annihilates with an electron of the surrounding tissue. Two back-to-back photons with an energy of $511\,\mathrm{keV}$ are emitted. The photons escape the body and are collected in radially arranged detectors (see figure 12).

The annihilation photons are detected via their interaction in scintillation crystals. The photons interact with the crystal through the photoelectric effect, the resulting electrons loose their energy through ionization. Part of the scintillation light emitted due to the relaxation of the excited crystal atoms propagates to the end of the crystal where it is detected. If two crystals have a signal at the same time, it is assumed that the corresponding photons originate from the same positron annihilation. The volume between the two crystals contains the position where the annihilation occurred. The superposition of many events allows to determine the distribution of the active substance in the body.

The resolution of the reconstructed isotope distribution is limited due to several factors. The emitted positrons have a certain range in the tissue before annihilation. This range depends on the kinetic energy of the positron and therefore on the isotope. For the two most used isotopes ^{18}F and ^{11}C the range is $0.54\,\mathrm{mm}$ and $0.92\,\mathrm{mm}$, respectively[7]. Another limitation comes from the noncollinearity of the two annihilation photons. The angle between the photons is $180 \pm 0.25\,^\circ$, which reduces resolution depending on the radius of the detector. In standard PET systems, the location of the photoelectric effect within the crystal is not known. This so-called depth of interaction (DOI) problem restricts the resolution depending on the distance to the detector axis: positron annihilations close to the detector axis are detected in two opposite crystals for which the reconstructed volume of possible annihilation positions is small. Events away from the detector axis may be detected in non-opposite crystals leading to a larger reconstructed volume. See figure 12 for an illustration.

It has further to be taken into account that annihilation photons may scatter before being detected. The dominant scattering process is Compton scattering

Radioactive isotope

Annihilation position

Crystal absorbing an
annihilation photon

Reconstructed annihilation
volume
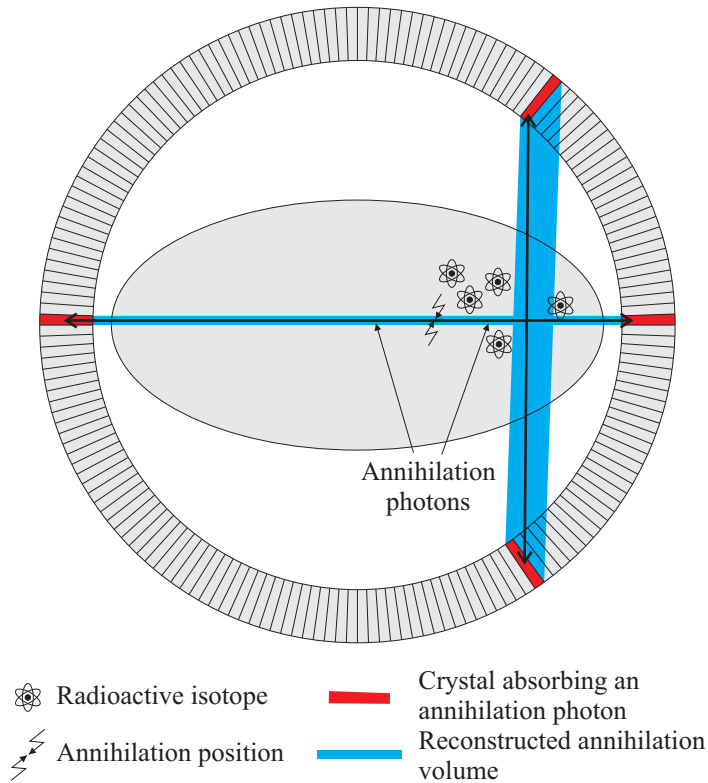
Figure 12: Principle of a PET detector. The two back-to-back photons interact in crystals (red) of the detector ring. The extent of the reconstructed volume where the annihilation could have occurred (blue) depends on the relative position of the two crystals since the position of the photon interaction within the crystal is not known (DOI problem).

where the photon looses part of its energy. Since the amount of light produced in the crystals allows the reconstruction of the energy of the detected particle, those events can be rejected.

3.1.3 The AX-PET project

The AX-PET collaboration studies and develops a setup of detectors with a different crystal configuration which overcomes the DOI problem. The scintillation crystals are not pointing in the direction of the patient, but are aligned parallel to the patient (i.e. in axial direction, see figure 13). The depth of interaction is now determined by the position of the crystal where an interaction is detected. The missing z-coordinate in the direction of the crystal is read out by placing thin plastic strips between the crystals. Some of the scintillation light does not propagate to a crystal end but escapes the crystal and enters the plastic strips where it is absorbed. The plastic is a wavelength shifting (WLS) material which reemits photons isotropically at a different wavelength. This light is detected at one end of the WLS strip. From the comparison of the signals in multiple

WLS strips placed orthogonally on the crystals, the interaction point of the annihilation photon can be reconstructed.

The readout of the crystals and the WLS strips uses G-APDs (see chapter 1). The setup is expected to allow building modules for PET scanners with excellent spatial, timing and energy resolution[8]. This paper presents a few of the central characteristics necessary to describe the modules such as the energy resolution, the number of detected photons from the crystals and the WLS strips and the distribution of the photons on the strips.

The aim of the AX-PET project is to build a demonstrator detector to demonstrate the improved performance compared to other PET systems. Further the setup will be used for the testing and calibration of the software simulation of the setup.

The setup used for the measurements presented here is not the demonstrator detector but a simplified setup using one LYSO crystal and seven orthogonal WLS strips read out with G-APDs.

3.2   Setup

A setup consisting of a long LYSO scintillation crystal ($3 \times 3 \times 100 \, \mathrm{mm}^3$) and seven orthogonal WLS strips ($3 \times 1 \times 40 \, \mathrm{mm}^3$) is used. The crystal and the WLS strips are coated with a reflective aluminium layer at one end, at the other end they are read out by Hamamatsu MPPCs. The optical contact is improved by using optical grease. A radioactive source (Na-22, $195 \, \mathrm{kBq}$) is placed in front of the crystal. On the opposite side of the source, a second crystal which is attached to a photomultiplier tube is used to select back-to-back photons (see figure 15).

3.2.1   MPPCs and PMT

Eight Hamamatsu MPPCs are used in the setup. The seven MPPCs used for the WLS strips readout are of the type MPPC-33-050C 7063. The MPPC attached to the LYSO crystal comes from a newer production series with the serial number S10362-33-050C. The properties of the two production series are assumed to be comparable to the series PSI-33-050C, which is the type of the diode that was analyzed in the first part of this paper. All diodes have a sensitive surface of $3 \times 3 \, \mathrm{mm}^2$ with 3600 pixels ($50 \times 50 \, \mu\mathrm{m}^2$ each). Particularly the values for the crosstalk and afterpulses corrections are taken from chapter 2: $\mu_{ct} = 10.9 \pm 1 \, \%$ for the crosstalk and $\mu_{ap} = 10.3 \pm 1 \, \%$ for the afterpulses.

The coincidence crystal is read out by a Hamamatsu Photomultiplier Tube H8443. The photomultiplier is run at an input voltage of $14 \, \mathrm{V}$ and a control voltage of $1.4 \, \mathrm{V}$.

The bias voltage of the MPPC attached to the LYSO crystal is provided using a Keithley power supply. Voltage selection is possible in steps of $0.05 \, \mathrm{V}$, the voltage closest to the Hamamatsu value is used. For the other seven MPPCs, a Fluke High Voltage Power Supply 815B is connected to a Oltronix voltage divider. The Fluke power supply is run at $69.6 \, \mathrm{V}$. The voltage divider allows the analog regulation of the input voltage on up to ten channels.
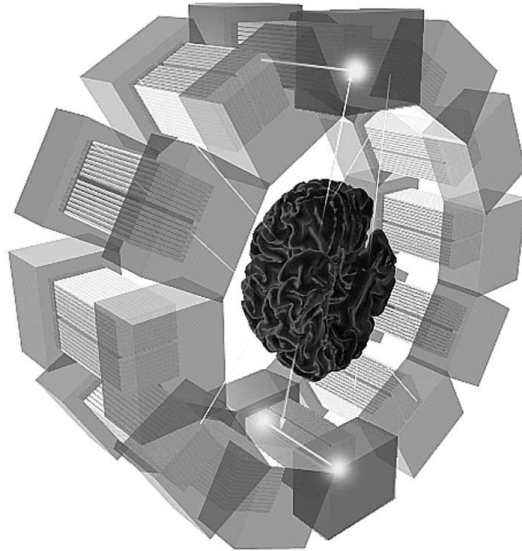
Figure 13: Setup of the AX-PET modules. The crystals are aligned parallel to the patient in the so-called axial direction. Picture taken from [9].
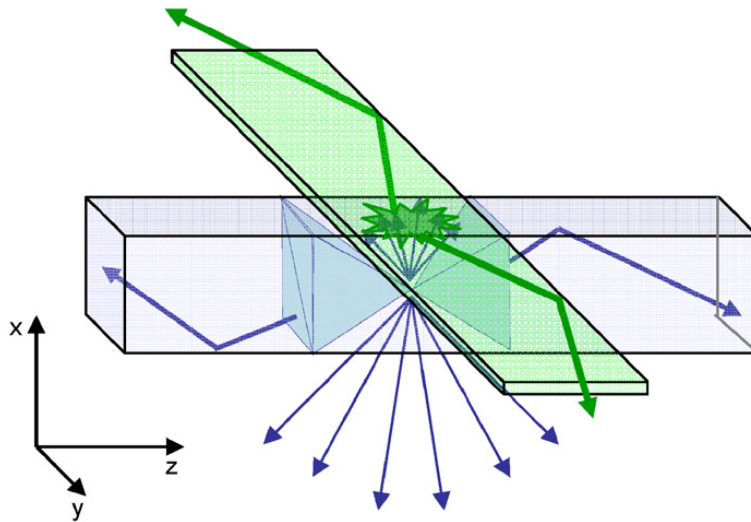
Figure 14: Principle of the z-axis readout. Some of the scintillation light escapes the crystal (blue) and enters the wavelength shifting strips (green, only one strip is showed). The light is absorbed and isotropically emitted at a different wavelength, which is the light detected at one end of the WLS strip. Picture taken from [8].
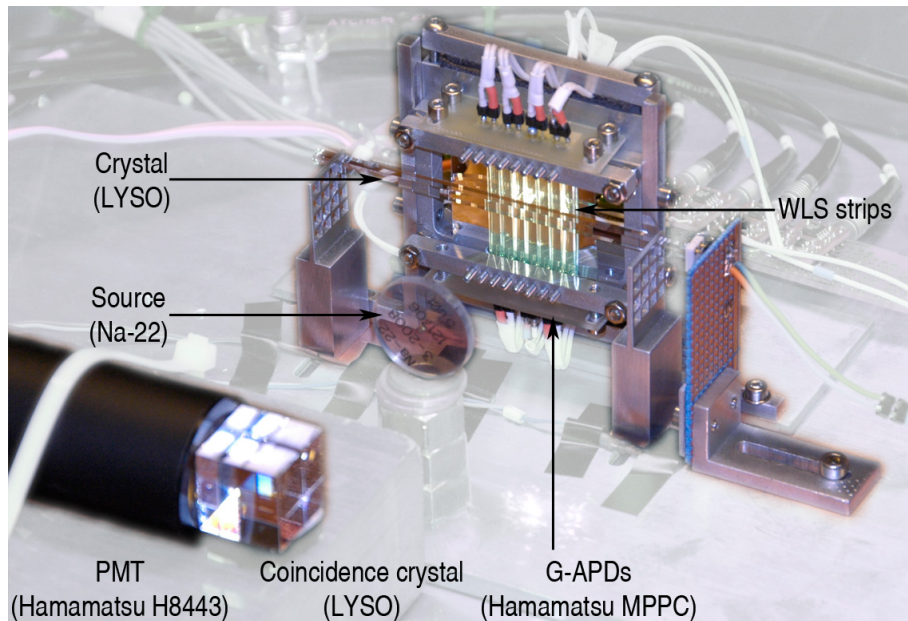
Figure 15: Overview of the setup.

3.2.2 Mechanics

The WLS strips and MPPCs are mounted on an aluminium construction. All pieces were drawn in CAD, manufacturing was done by C. Haller (ETH Zurich). The gap between two WLS strips is 0.2 mm. The MPPCs are mounted on a carrier board, alternatively on top and below the WLS strips. On the other side of the WLS strip a soft foam pushes the WLS strip to the MPPC. The WLS strips are installed with an alternating shift of ± 1 mm in longitudinal direction with respect to each other. Behind the WLS strips a reflective foil (Vikuiti Enhanced Specular Reflector by 3M[3]) is mounted to increase the amount of light from the crystal absorbed in the WLS strips. To ensure total internal reflection in the WLS strips, a wire with a diameter of $150\,\mu$m is placed between the foil and the WLS strips. The strips are fixed with grub screws, which are only loosely tightened to avoid damage to the strips. A front view of the WLS strip and MPPC mounting is shown in figure 16.

3.2.3 Temperature stabilization

Since the MPPCs are sensitive to temperature variations, the setup is placed on a copper plate connected to a water cooling unit. A polystyrene box over the setup ensures further temperature stabilization. This setup allows to keep the temperature stable within $0.05\,°$C.

---

[3]www.3m.com
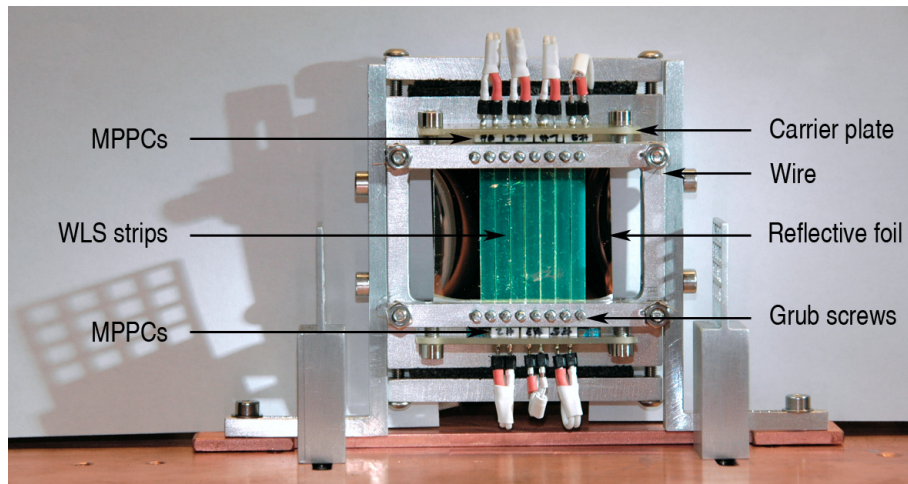
Figure 16: Front view of the WLS strip and MPPC mounting.

3.2.4 Source

The Na-22 isotope has two decay modes, β^+ with a probability of $90\,\%$ and electron capture ($10\,\%$). Annihilation of the positron leads to two back-to-back photons with an energy of $511\,$keV. Another photon with an energy of $1.275\,$MeV is emitted due to the decay of the unstable Ne-22m (half-life $3.7\,$ps) to which both decays lead.[10]

3.2.5 Crystals

AX-PET uses PreLude 420 scintillation crystals from Saint-Gobain[4]. PreLude 420 is a Cerium doped Lutetium Yttrium Orthosilicate crystal ($Lu_{1.8}Y_{0.2}SiO_5$:Ce, usually referred to as LYSO). According to the product description provided by the manufacturer, the attenuation length for $511\,$keV-photons is $1.2\,$cm. The photon yield is $32\,$photons/keV with a peak wavelength of $420\,$nm (blue light). At this wavelength the refraction index is 1.81. The decay time is $41\,$ns.[11]
The effective attenuation length of the emitted light is $42.0 \pm 0.9\,$cm.[12]
The light yield of the $511\,$keV-photons may be reduced by $54.04\,$keV due to the lutetium X-ray escape peak[13]. This escape peak has to be taken into account when energy spectra measured with LYSO crystals are analyzed.
Even for particles with identical energy, the amount of scintillation light varies. The so-called intrinsic resolution is $7\,\%$ (FWHM)[14].

3.2.6 Wavelength shifting strips

Wavelength shifting (WLS) strips consist of organic plastics. They absorb light at a certain wavelength and re-emit it at a longer wavelength. AX-PET uses BC-482A strips from SaintGobain. The absorption peak at $420\,$nm matches the wavelength of the light emitted from the LYSO crystals. The emission peak is at

---
[4]www.detectors.saint-gobain.com
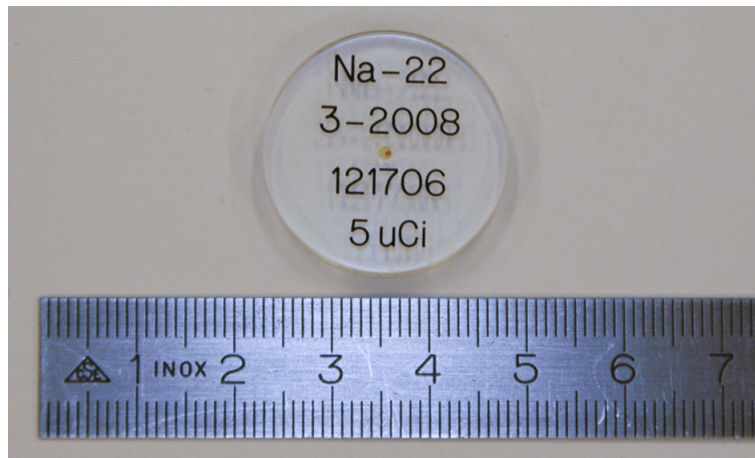
Figure 17: The used Na-22 source. Note the different color shades in the center of the source, which suggests a non-uniform activity in the active area.

494 nm. The light attenuation length is 400 cm (all values from the SaintGobain product specification[15]).

The used WLS strips have a length of 4 cm. The WLS strips are read out alternately above and below the crystal (see section 3.2.2). The crystal is only roughly in the middle of the strips (precision approximately 5 mm), but since the light attenuation length is much longer this error is neglected.

3.2.7 Electronics: Overview

The signals from the nine photodetectors have to be processed such that given a certain criterion all signals are integrated in an ADC (Analog-to-Digital Converter) which is connected to a readout computer. The criterion is for example the simultaneous interaction of two (back-to-back) photons in the long crystal and the coincidence crystal. The circuit for this selection is called the trigger logic.

The two pins of each MPPC are connected with short coaxial cables ($< 10\,\text{cm}$) to the amplifier. The screens of the cables are connected at both ends. At the amplifier end they are additionally connected to the amplifier ground. One cable is connected to the bias voltage, the other carries the signal and leads to the input of the operational amplifier.

The signals from the MPPC attached to the crystal and the PMT attached to the coincidence crystal are split and used for the trigger logic. The trigger circuit outputs the integration gate for the ADC. Since the processing in the trigger circuit needs time, the ADC input signals have to be delayed. The signals from the MPPC attached to the crystal and the PMT are attenuated to match the range of the ADC. A block diagram of the electronics is shown in figure 19.
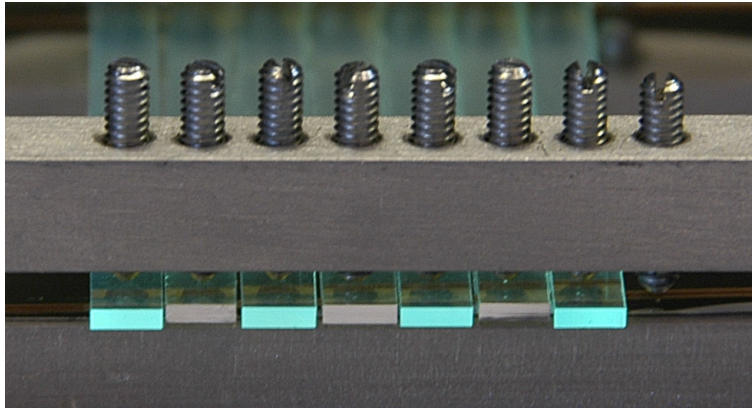
Figure 18: Picture of the installed WLS strips before the MPPCs are added. Every second strip is coated with aluminium.

3.2.8 Electronics: Amplifier

The amplifier was designed by A. Rudge (Ohio State University) and uses the OPA842 and OPA846 operational amplifiers by Texas Instruments[5] in a non-inverting amplifier circuit. The two chips have very similar properties, except that the OPA846 has the larger gain bandwidth product which makes it faster (1750 MHz instead of 400 MHz[16][17]). Due to the limited availability of OPA846 chips, only the channel used for the trigger (channel 7) and one additional channel (channel 4) feature the OPA846 chip, the other six channels use the OPA842 chip. The amplifiers were assembled by L. Djambazov (ETH Zurich).

The eight amplifiers have a common voltage supply of +5 V and -5 V and a common grounding which is connected to the ground of the voltage supply. Each amplifier has a separate coaxial cable for the bias voltage of the MPPC and a LEMO connector for the signal output. Two short coaxial cables lead to the pins of the MPPC. The screens of the two cables are connected at the MPPC end and connected to the amplifier ground at the other end. Using only one coaxial cable with the bias voltage on the screen and the signal in the core was tested but showed worse noise properties.
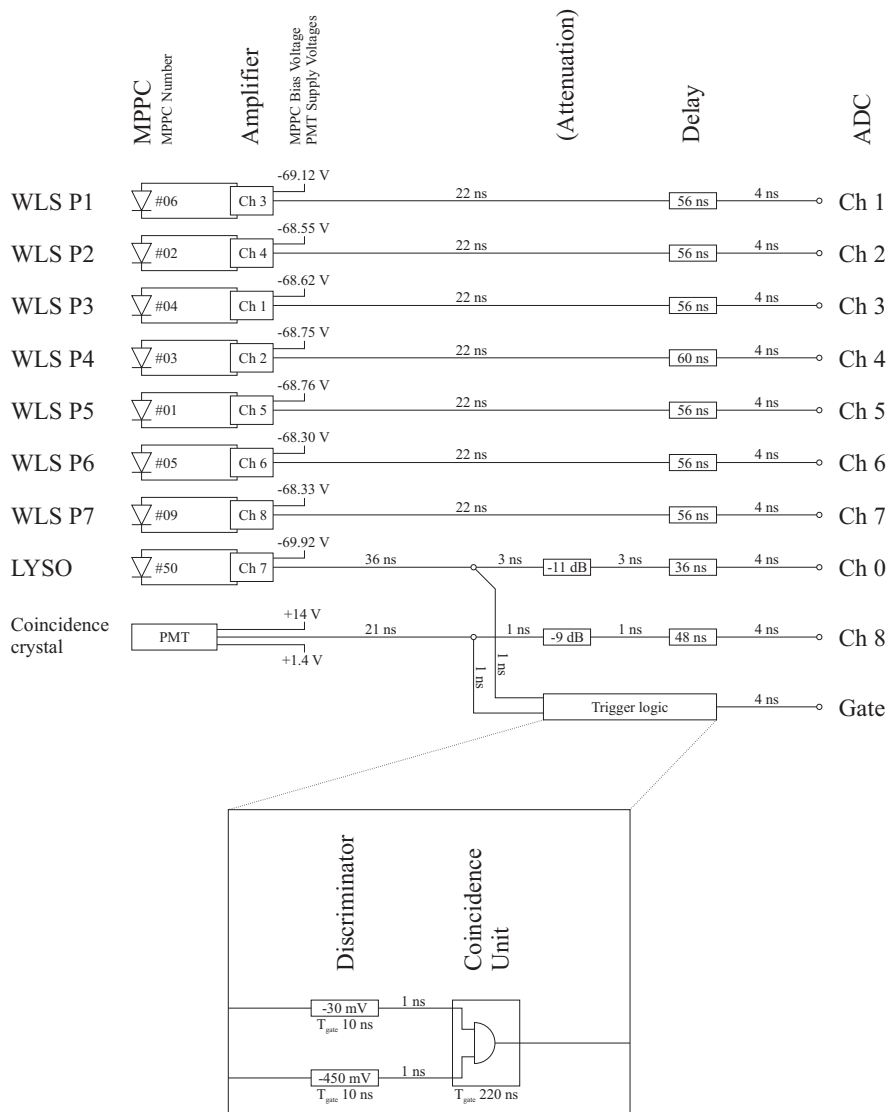
The gain of the amplifier is defined by the two resistors R3 (470 Ω) and R2 (50 Ω) in the circuit diagram (figure 20). For a non-inverting amplifier circuit the gain is given by $G = 1 + \frac{R3}{R2} = 10.4$.

3.2.9 Electronics: Trigger

The signals from the two crystals are used to define the criterion when to start data taking. The goal is to select events where a 511 keV-photon interacts in the long crystal and another in the coincidence crystal.

Both signals are split using a 50 Ω-splitter. The signals are then discriminated in a LeCroy 821CS Quad Discriminator. The discriminator threshold for the long LYSO crystal is -30 mV, the lowest possible setting. For a correct geometric

---

[5]www.ti.com

MPPC
MPPC Number

Amplifier

MPPC Bias Voltage
PMT Supply Voltages

(Attenuation)

Delay

ADC

WLS P1	#06	Ch 3	-69.12 V	22 ns	56 ns	4 ns	Ch 1
WLS P2	#02	Ch 4	-68.55 V	22 ns	56 ns	4 ns	Ch 2
WLS P3	#04	Ch 1	-68.62 V	22 ns	56 ns	4 ns	Ch 3
WLS P4	#03	Ch 2	-68.75 V	22 ns	60 ns	4 ns	Ch 4
WLS P5	#01	Ch 5	-68.76 V	22 ns	56 ns	4 ns	Ch 5
WLS P6	#05	Ch 6	-68.30 V	22 ns	56 ns	4 ns	Ch 6
WLS P7	#09	Ch 8	-68.33 V	22 ns	56 ns	4 ns	Ch 7
LYSO	#50	Ch 7	-69.92 V	36 ns	3 ns / -11 dB / 3 ns	36 ns	4 ns	Ch 0

Coincidence crystal — PMT — +14 V / +1.4 V — 21 ns — 1 ns / -9 dB / 1 ns — 48 ns — 4 ns — Ch 8

1 ns   1 ns

Trigger logic — 4 ns — Gate

Discriminator

Coincidence Unit

-30 mV
T_{gate} 10 ns — 1 ns

-450 mV
T_{gate} 10 ns — 1 ns

T_{gate} 220 ns

Figure 19: Block diagram of the electronics. The two signals from the crystals are split and taken in coincidence for the trigger. All nine signals are integrated in the ADC, the resulting data is saved event by event. The indicated bias voltages are the suggested values provided by Hamamatsu.
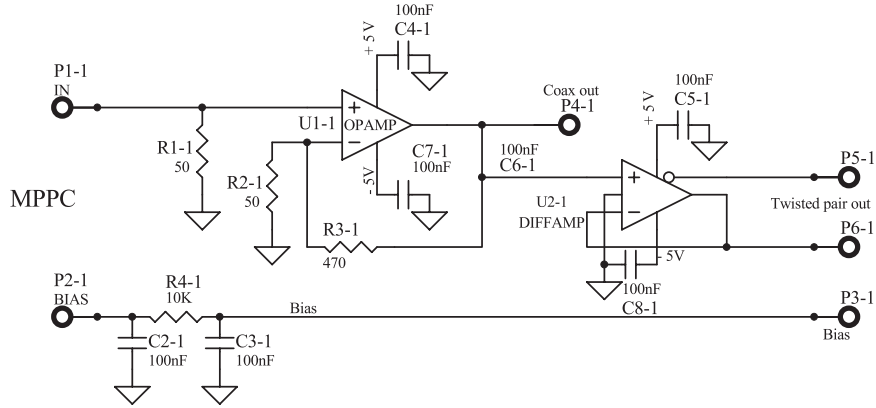
Figure 20: Circuit diagram of the amplifier.

selection it is necessary to sort out events where one or both photons were Compton scattered. This criterion can be realized during data analysis since the deposited energy for both crystals is read out. Nonetheless, for the coincidence crystal a higher threshold is chosen to cut away Compton events. The 511 keV-peak is at -500 ± 30 mV, the threshold is set to -450 mV.

The timing difference between the two channels is the result of the differences of the photodetectors and thresholds (a leading edge discriminator was used). The MPPC signal is 15 ns faster than the PMT signal, and is therefore delayed using longer cables. The time jitter between the two signals is 5-10 ns, hence the gate lengths of the discriminators are set to 10 ns.

Coincidences between the two binary signals are detected using a LRS 465 Coincidence Unit.

3.2.10 Electronics: ADC

The signals are integrated using a Caen V792[6] Analog-to-Digital converter (ADC). The V792 module features 32 channels with $50\,\Omega$ impedance. Negative input signals from 0-400 pC are allowed. An A392 flat cable to LEMO input adapter is used. The integration gate is set by a common NIM signal on a LEMO connector. All technical specifications are taken from the product manual[18].

The V792 is a module for VME crates. For every gate all active channels are integrated and the digital data saved for readout. The buffer can store up to 32 events. Readout and configuration of the module is done via the VME interface. Each channel can be set to active or inactive, and an underflow value can be set below which the channel data is not saved for readout. During the conversion of an event (approximately $7.5\,\mu$s) the module ignores further events. Thus pile-up is not a problem for the V792.

The module allows to set a pedestal current common to all channels to correct for baseline shifts in the input signals. The maximal pedestal current is $92.2\,\mu$A which corresponds to a baseline shift of $+4.6$ mV. The input signals from the

---

[6]www.caen.it

amplifiers have a baseline shift between -11 mV and +6 mV. The negative baseline shifts are no problem since the dynamic range of the ADC is larger than needed for the WLS strip signals. The positive shifts are corrected by setting the pedestal current to the highest possible value. Amplifier channel #3 has a baseline shift of +6 mV and cannot be corrected. The corresponding WLS strip P1 is excluded from the analysis, only six WLS strips remain.

The integration gate must precede the signal by at least 20 ns. The gate length is determined using an estimation of the signals: the peaking time and the decay time constant of the signals are approximately 40 ns. Including four decay lengths includes more than 98 % of the signal. The total gate length is set to $(20 + 40 + 4 \cdot 40 = 220)$ ns. Note that the effective gate length used for the afterpulses correction does not include the 20 ns of the gate preceding the signal.

3.2.11 DAQ

The V792 module is read out by a VME controller module with CERN Scientific Linux[7] installed. The ATLAS VME driver is used.

The VME modules can be accessed using the application programming interface (API) of the driver. A library was written which allows the complete configuration of the V792 module. A second library was written for the Caen V812 module, a 16 channel constant fraction discriminator. The V812 module was not used in the final setup. Both libraries were integrated into a command line user interface. The interface is able to manage multiple V792 and V812 modules and accepts script files for the automatization of the device configuration. The communication with the VME crate is established at program startup. For each module type an address file containing the base addresses of the available modules is read. For each module the communication is tested, on success its number and status reported.

The V792 module can be read out by a simple run routine. Three parameters are necessary: the number of the V792 module (as shown at program startup), the run number and the number of events to be read. The binary data stream from the module is saved to a data file without any processing. The data is organized in 32-bit words. An event consists of a header word, one for each active channel containing its ADC value, and an End of Block (EOB) word. See the product manual for details on the raw data format[18]. A separate program converts the binary data file to an ASCII file which contains the ADC data in plain text.

3.3 Source spectrum and LYSO light yield

3.3.1 Method

The setup is as described in chapter 3.2. An MPPC is attached to the first, long LYSO crystal, a PMT to the second one with the source in between. The MPPC is carefully attached to the LYSO crystal using optical grease. The Na-22 spectrum is measured using the integration function of the oscilloscope (LeCroy Waverunner LT584). The integration gate length is 200 ns.

The temperature is constant $\pm 0.05 \, ^\circ$C during the measurements.

---

[7]linux.web.cern.ch/linux/scientific4/

The histogram from the oscilloscope is fitted using a Gaussian curve for the 511 keV-peak. A second Gaussian curve at a 54.07 keV lower energy is used for the lutetium escape peak. The slope of the Compton edge is approximated using an exponential curve. The ansatz is taken from P. Solevi (2007)[19].

$$f(M) = C_0 e^{-\frac{M-\mu}{2\sigma^2}} + C_1 e^{-\frac{M-\left(\frac{511-54.07}{511}\right)\mu}{2\alpha^2}} + C_2 e^{-\frac{M-\nu}{\beta}} \tag{3.1}$$

Other fit curves such as a Gaussian curve with a linear or polynomial underground were tested, but the results are not stable to variations in the initial values of the fit algorithm and the fitted histogram range.

The energy resolution is calculated using the standard deviation σ and mean value μ from the 511 keV-peak. Since the number of breakdowns $\tilde{N}$ is linear to the signal strength in ADC counts, the energy resolution is

$$\frac{\Delta \tilde{N}}{\tilde{N}}(FWHM) = \frac{2\sigma\sqrt{2ln(2)}}{\mu}. \tag{3.2}$$

The charge of one cell is measured by sending a weak light pulse to the MPPC. In difference with the Poisson method used for the determination of the crosstalk rate (section 2.3.3), the full signal is integrated. The position of the 511 keV-peak is now converted into a number of breakdowns by dividing the corresponding charge by the charge of a single breakdown. The ADC to charge conversion factors are 4 pC/count for the spectrum and 0.02 pC/count for the single cell measurement.

Using the equations (1.7),(1.8),(1.10) and (1.11) on page 7, the corresponding number of detected photons N_{pe} is calculated. The values used for crosstalk and afterpulses corrections are $\mu_{ct} = 10.9 \pm 1\%$ and $\mu_{ap} = 10.3 \pm 1\%$ according to section 3.2.1.

3.3.2 Results

The calibration measurement has an error of 4 %, the error of the 511 keV-peak position is negligible. The difference between the peaks in the calibration spectrum is 21.07 ± 0.85 ADC counts, therefore the charge of one cell is 0.4214 ± 0.02 pC. In the source spectrum the pedestals are subtracted. The peak position is at 138.1 ADC counts corresponding to a charge of 552.4 pC. Using those two values the number of breakdowns within the gate is $\tilde{N} = 1311 \pm 53$. The corresponding number of detected photons is $N_{pe} = 1320 \pm 68$. The energy resolution of the spectrum is $\frac{\Delta E}{E}(FWHM) = 11.4\%$.

3.3.3 Discussion

The energy resolution (FWHM) was measured at 11.4 %. The calculation of an expected value according to equation (1.16) is not possible since σ_{N_0} is correlated to the intrinsic resolution of the crystal.

A. Braem *et al.* (2008)[20] estimates the number of breakdowns at 1317 for a 511 keV-event. The stated crosstalk correction of 20 % relates to the combined correction for crosstalk and afterpulses in the analysis above which is $(1 + \frac{3600-1300}{3600} \cdot 0.109)(1 + 0.103) - 1 = 18\%$. From the reference value the number of detected photons is calculated as $N_{pe} = 1309$. The measured value of 1320 ± 68 detected photons is in good agreement.
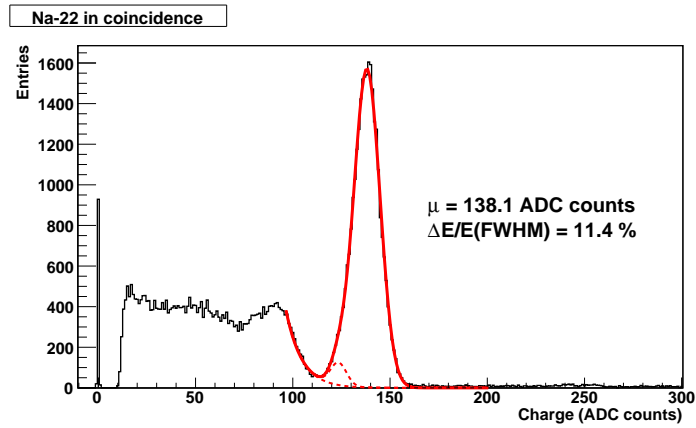
Figure 21: Na-22 spectrum measured with a MPPC attached to a LYSO crystal. The spectrum is measured in coincidence with a second crystal. The red line is the fitted curve (equation (3.1)), the dotted line shows the contributions from the Compton edge and the lutetium escape peak. The 511 keV-peak corresponds to 1320 detected photons.
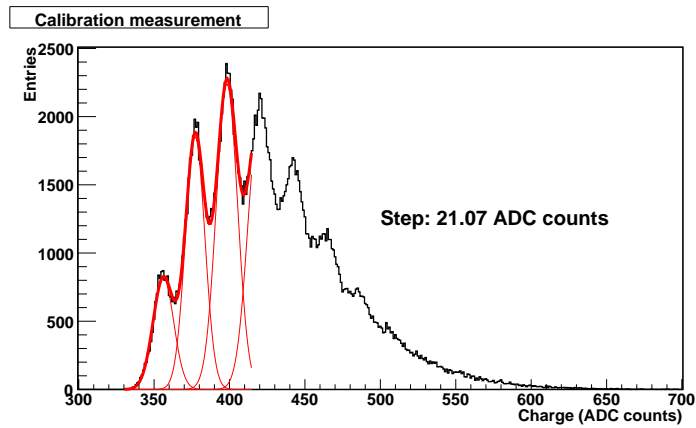
Figure 22: Calibration of the MPPC with single photon signals. The ADC to charge conversion factor is not identical to the Na-22 spectrum measurement.

3.4 Light loss by adding a glass window

The MPPCs are delivered with a soft silicoloid layer on top of the chip for protection. For the demonstration module, a hard surface is preferred to simplify the installation. A thin glass is glued on top of the diode. This leads to a light loss which has to be measured.

3.4.1 Method

The method to determine the light loss is to compare the number of detected photons of 511 keV-events for a diode without and with glass window. The measurement without glass window is presented in the previous chapter. The measurement of the diode with glass window uses the same method as presented above.

3.4.2 Results

The spectrum is shown in figure 23. The ADC to charge conversion factors are 2 pC/count for the spectrum and 0.02 pC/count for the single cell measurement. The peak is at 253.9 ADC counts (507.8 pC). The calibration measurement is made 0.3 °C below the temperature of the other measurements (temperature stabilization (section 3.2.3) not yet available). A temperature correction is made using the values from chapter 2.2 and [2]. The uncorrected peak difference in the calibration spectrum is 21.68 ± 0.87 ADC counts, including the temperature correction the peak difference is 21.01 ± 1.1 ADC counts (0.4202 ± 0.03 pC).
The number of detected breakdowns is 1209 ± 64. Using 10.9 % crosstalk, 10.3 % afterpulses and including saturation, the number of detected photons is 1195 ± 78. The relative light loss is 9.5 ± 0.8 % compared to the measurement without glass window.
A simulation by C. Joram (CERN, Geneva) yields a light loss of 9 %. A calculation using only geometrical optics is presented in appendix A. The calculated light loss is 8.8 %. The measurement is in agreement with the simulation and the calculation. The energy resolution is decreased by 0.3 % due to the light loss.

3.4.3 Discussion

The light loss from the measurement, the calculation and the simulation are in good agreement at approximately 9 %. Unfortunately, a lower light loss was presented at an earlier time. The light loss presented was 3.7 % using the calibration with the single cell charge. Using the difference in the energy resolution a light loss of 9.1 % was estimated. The light loss from the calculation was stated to be 4 % for photons reaching the crystal-diode intersection at the center of the crystal. This value is correct, but to estimate the light loss the integral over the area has to be calculated, which has not been done at that point.
The difference in the analysis of the measurement has two reasons. The peak difference in the calibration measurements was not determined using a fitted curve, but by estimating the peak differences directly from the spectrum. The calibration value of the diode without window was 5 % too high. This is within the stated error range but lead to a large error in the difference between the measurements without and with glass window.
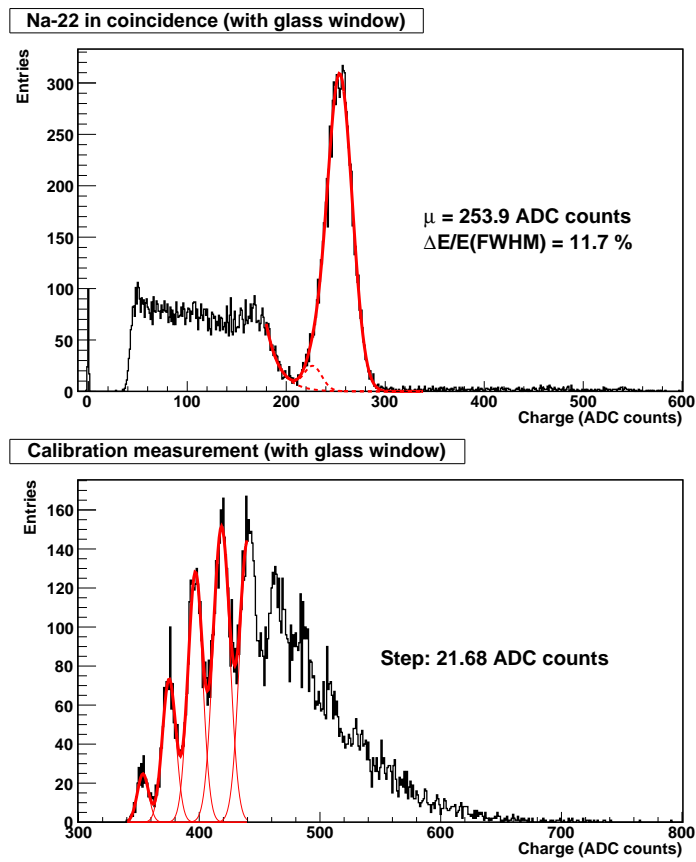
Figure 23: Na-22 and calibration spectrum of the MPPC with glass window. The 511 keV-peak corresponds to 1195 detected photons.

The second reason is a difference in the calculation of the number of detected photons from the number of breakdowns. The used method first corrects saturation before subtracting crosstalk and afterpulses. As shown in chapter 1.5, crosstalk and afterpulses have to be subtracted before the saturation correction.

3.5 WLS strips calibration

3.5.1 Method

The signals of the MPPCs attached to the WLS strips vary relatively to each other. Even when the same amount of light reaches two different WLS strips, the signals from the MPPCs will not be the same. Since the z-coordinate is calculated by comparing the relative signals in the WLS strips, the WLS strips have to be calibrated.

Beside statistical effects, two main factors lead to differences. First the bias voltage is not precisely known. The used configuration allows to set the bias voltage with a precision of only $0.1\,\mathrm{V}$, which leads to differences in the gain of up to $10\,\%$. The second factor is the unknown quality of the contact between WLS strip and MPPC.

The idea is to calibrate the strips by taking the coincidence crystal close to the source such that coincidence events cover the full length of the crystal in front of the strips. For each event the signal in the long LYSO crystal, the coincidence crystal and the seven WLS strips are measured in the ADC. Pedestals are taken by sending random signals to the unit which creates the ADC gate, thus ensuring the precisely same gate length. Only events which deposit $511\,\mathrm{keV} \pm 3\sigma$ in the crystal are selected (described in section 3.6). The signal spectrum of a single strip is assumed to show a large amount of small signals when the photon energy is deposited in the crystal away from this strip, and a smaller amount of larger signals when the energy deposition is close to or in front of the strip. The upper edge of the distribution relates to signals when the interaction is in front of the strip. The position λ of the edge (in ADC counts) is a measure of the combination between contact quality and gain.

To determine this position a fit is applied to the data which reproduces the distribution. The fit is the superposition of two Gaussian curves and a "box function" with rounded edges.

$$f_{\mathrm{WLS}}(x) = \underbrace{C_0 e^{-\frac{x-\mu}{2\alpha^2}} + C_1 e^{-\frac{x-\nu}{2\beta^2}}}_{\text{Gaussians}} + \underbrace{\frac{C_2}{(e^{-(x-\tau)/\gamma} + 1)(e^{(x-\lambda)/\delta} + 1)}}_{\text{box function}} \qquad (3.3)$$

Normalized units (n.u.) are defined, the WLS signals are linearly scaled such that the upper edge is at $1600\,\mathrm{n.u.}$ The one cell signal is measured using the pulsed LED.

3.5.2 Results

The positions of the upper edges are listed in table 4. For most strips, the position is at approximately $1600\,\mathrm{ADC}$ counts. Only the edge of strip number 5 is significantly lower at $801.8\,\mathrm{ADC}$ counts. The MPPC gain is comparable to the gain of the other MPPCs. It can therefore be assumed that the signal loss is due to the alignment of the strip on the MPPC. The strip with the best

Strip number	1	2	3	4	5	6
Strip label	P2	P3	P4	P5	P6	P7
Edge position λ_i						
ADC counts	1967.7	1615.6	1332.6	1647.6	801.8	1663.8
charge (pC)	196.8	161.6	133.3	164.8	80.2	166.4
normalized units	1600					
Single breakdown						
charge (pC)	1.54	1.50	1.49	1.52	1.61	1.51
normalized units	12.5	14.8	17.9	14.8	32.1	14.5
relative error (%)	3	3	3	7	7	7

Table 4: Calibration of the WLS strips. The position of the edge is used to define normalized units (n.u.), the charge per breakdown is used later for the calculation of the light yield per strip.

alignment and therefore the best light yield is strip number 2, where a single cell corresponds to 12.5 n.u. For later calculations of the number of breakdowns, this strip is used.

3.5.3 Discussion

The position of the upper edge in the spectrum of the signals is a simple measure of the combination between contact quality and gain of the MPPC. The normalized signals can be used for the coordinate reconstruction of events.
The uncalibrated signal from WLS strip number 5 is significantly lower than that from the other strips. It was found that the MPPC attached to this WLS strip was slightly inclined relatively to the other MPPCs. During installation, the effect was estimated to be small. It can be concluded that even small deviations in the alignment lead to a significant light loss.

## 3.6 Event selection and summed WLS strips light yield

3.6.1 Method

Again the measurement where the photons are distributed over the crystal in front of all WLS strips is used. The WLS signals are normalized according to the previous chapter. From the data, events are selected where 511 keV are deposited in the crystal. The mean value and the standard deviation of the 511 keV-peak are determined using the standard fit curve (equation (3.1)). An energy cut is made at $\mu \pm 3\sigma$.
The cuts should further select events where the energy deposition is in front of the WLS strips. As a second cut events are selected where the largest signal is in one of the four inner strips, which cuts away events in front of one of the boundary strips and events beside, but close to the strips. The remaining events are either in front of the inner strips or far away from the strips where the determination of the largest signal is dominated by statistical fluctuations. In order to discern the two types of signals, the sum of the signals in all WLS strips is calculated. A third cut is made between the two categories.
The summed signal is further used to calculate the total light yield of all six WLS strips.
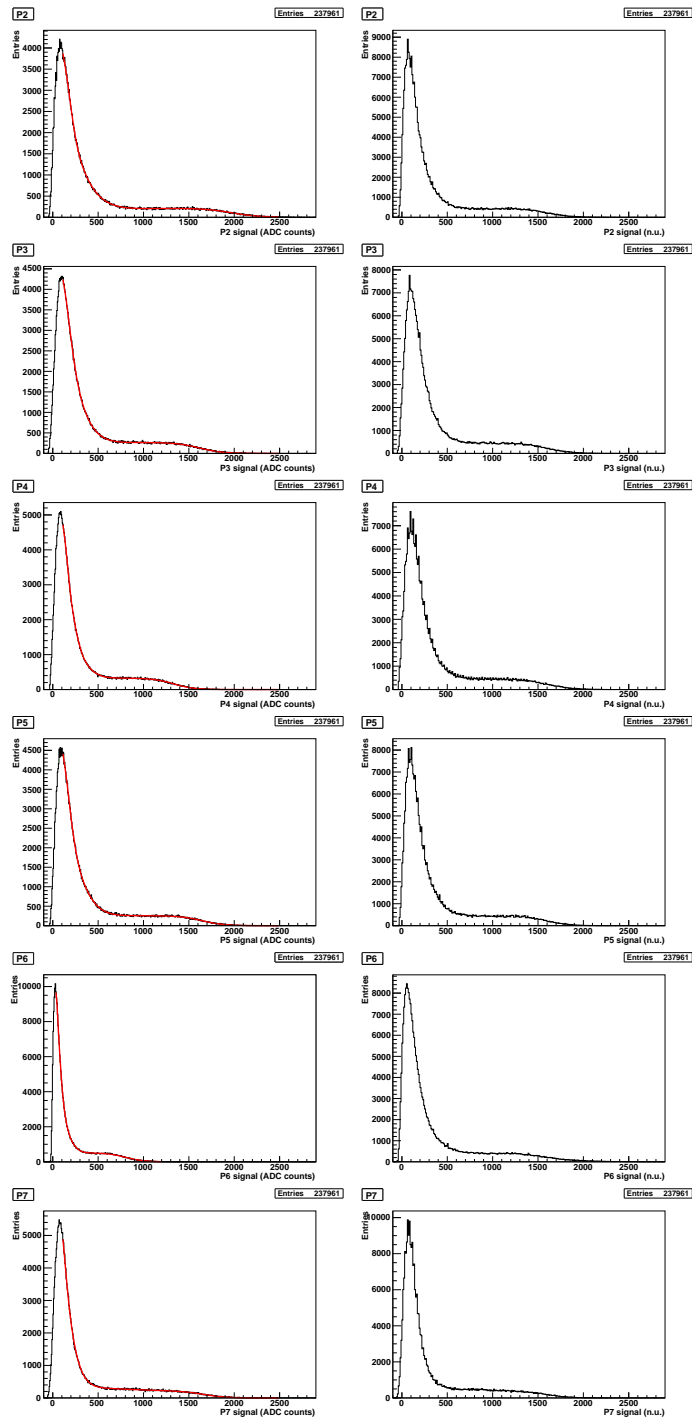
Figure 24: Calibration of the WLS strip signals. The upper edge of the spectrum is used as a measure of the combination between contact quality and gain. On the left are the histograms of the uncalibrated, on the right of the calibrated signals.
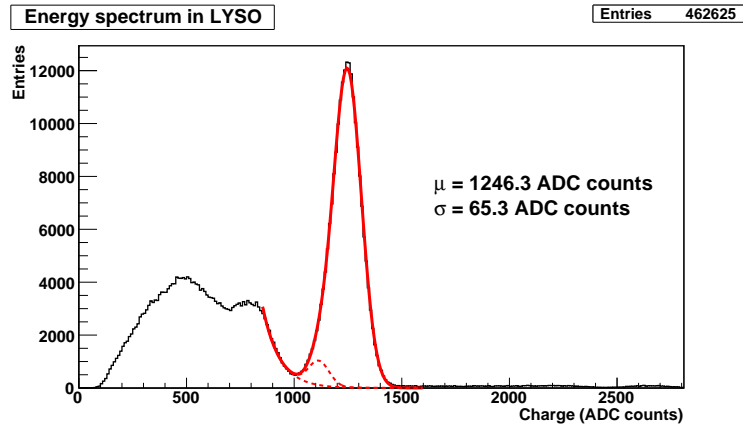
Figure 25: Determination of the position and width of the 511 keV-peak. The values are used to introduce cuts at 1050 and 1443 ADC counts.

3.6.2 Results

The spectrum in the LYSO crystal has an energy resolution of 12.3 %. The peak is at 1246.3 ADC counts and has a standard deviation of 65.3 ADC counts. These values are used for a first cut on the energy at 1050 and 1443 ADC counts. The histogram and the fitted curve are shown in figure 25.

After applying the energy cuts, events are selected where the largest signal is in one of the inner strips. The summed signal is filled into a histogram (figure 26). Two well-separated ranges can be discerned. A simpler fit is applied consisting only of an exponential and a Gaussian curve. Based on the mean value and the standard deviation of the Gaussian, the third cut is introduced at $\mu \pm 3\sigma$, i.e. at 1385 and 4178 n.u.

The peak of the summed WLS strips signal is centered at 2781.8 n.u. Depending on the WLS strip, this corresponds to a different number of breakdowns due to the varying contact quality. Using the value from table 4 of the strip with the best contact (number 2), the number of detected breakdowns is 223 ± 7, the number of detected photons is 182 ± 6.
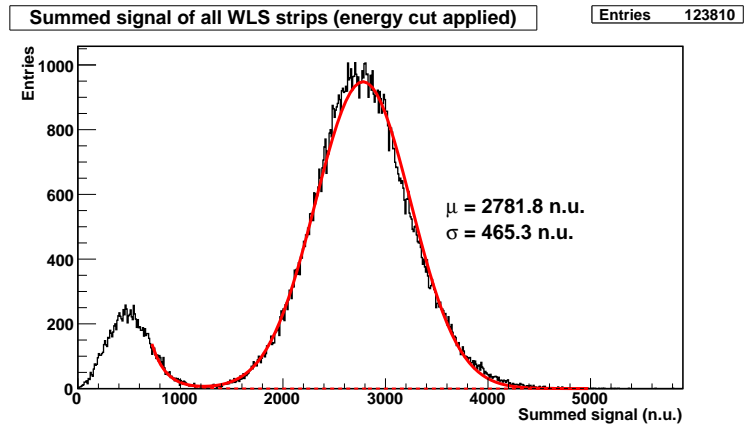
The signal in the crystal and the summed signal of all WLS strips have to correlate. This correlation can be seen in figure 27.

3.6.3 Discussion

The energy resolution is 12.3 %, which is lower than in previous measurements. A possible explanation is that the crystal-diode contact is very sensitive to vibrations. In the used setup vibrations can displace the crystal on the diode and worsen the distribution of the optical grease, both leading to light loss. Since the crystal was not reinstalled for the measurement, a non-optimal contact is the most probable reason for the reduced energy resolution.

The signal in the LYSO crystal and the WLS strips correlate. Events outside the correlation region (left part in figure 26, lower part in figure 27) are events in the crystal with the energy deposition beside the WLS strips. The total light

Figure 26: Determination of the cut on the sum of all WLS strip signals. The cuts are made at 1387 n.u. and 4177 n.u.
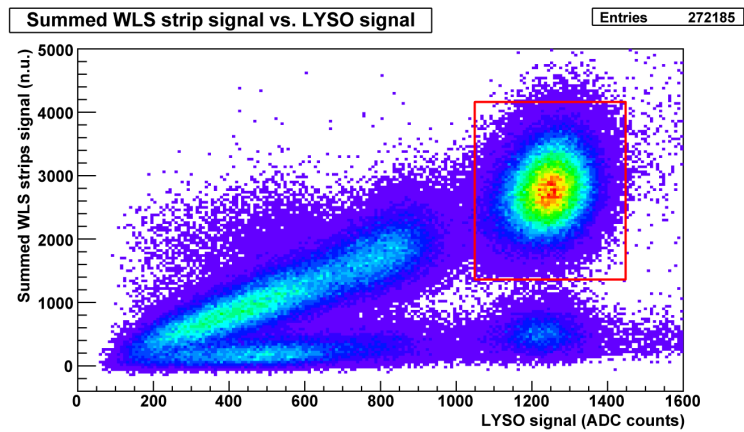
Figure 27: Correlation between the signal in the LYSO crystal and the summed signal of all WLS strips. The red box indicates the selected events for the further analysis (energy cut and cut on the summed signal). Only events with the maximal signal in one of the inner four strips are selected.

yield and the distribution of the light on the strips is discussed in section 3.8.

3.7 Evaluation of various reconstruction algorithms

The position of the interaction of the primary photon in the crystal can be reconstructed from the light distribution in the WLS strips. The primary attribute of different reconstruction algorithms is the standard deviation of the differences between reconstructed and original coordinates. Three different reconstruction methods are compared.

3.7.1 Method

Again the data from the same measurement series is used. The uniform distribution of the events in the crystal is explicitly used. The original coordinate of an event i is called z_i. The reconstructed variable r_i is not identical to z_i due to statistical and systematic errors. The statistical error depends on the light distribution in the WLS strips and the reconstruction algorithm. Even a perfect reconstruction algorithm without systematic errors would not return z_i but a shifted coordinate $\tilde{z}_i = z_i + \Delta z_i$. The difference between r_i and $\tilde{z}_i$ is the result of systematic errors. The function $r_i = r(\tilde{z}_i)$ is piecewise monotonic[8]. The evaluated reconstruction algorithms are further symmetric around the center of each strip within $[-d/2, d/2]$.

In this measurement series the event coordinates z_i are uniformly distributed over the length of the crystal in front of the WLS strips. Since Δz_i is a statistical error which is Gaussian distributed around zero, the coordinates $\tilde{z}_i$ are also uniformly distributed. Using the monotonicity of $r(\tilde{z}_i)$ it is possible to get the corresponding $\tilde{z}_i$ for each r_i by simply sorting the reconstructed variables.

One WLS strip is selected. The center of the strip is assigned to $z = 0$. The step size between two strips is d, which is the unit used for the analysis ($d = 3.2\,\mathrm{mm}$). All events with a reconstructed variable r_i within $[-d/2, d/2]$ are selected. The number of such events be E. Due to the translation symmetry $z \rightarrow z + d$ the corresponding $\tilde{z}_i$ must be in the same interval. For a sorted list of the reconstructed coordinates r_i the corresponding $\tilde{z}_i$ are given by

$$\tilde{z}_i = r^{-1}(r_i) = -\frac{d}{2} + \frac{i}{E}d. \tag{3.4}$$

It has to be noted that this assignment assumes the distances between the $\tilde{z}_i$ to be constant instead of being Poisson distributed. The error of this assumption is neglected since it is in the order of $\frac{d}{E}$, $E > 25000$.

The standard deviation of the systematic error of a reconstruction algorithm $r(\tilde{z}_i)$ is given by

$$\sigma_r^2 = \frac{1}{E} \sum_{i=1}^{E} (r_i - \tilde{z}_i)^2 \tag{3.5}$$

3.7.2 Reconstruction algorithms

The simplest reconstruction algorithm selects the WLS strip with the largest signal and uses the center position of this strip as the reconstructed coordinate.

---

[8]Note that besides statistical effects a reconstruction algorithm will not change the coordinate order of events, i.e. if $\tilde{z}_1 > \tilde{z}_2 \Rightarrow r(\tilde{z}_1) \geq r(\tilde{z}_2)$.

This algorithm will be referred to as "maximum" (max) algorithm. This algorithm has a small error for events close to the center of a strip and has its maximal error for events at the border between two strips. The expected value for the standard deviation is $\sigma_{max}^2 = \frac{1}{d} \int_{-d/2}^{d/2} x^2 dx = \frac{d^2}{12}$.

The "center of gravity" (COGx) algorithms select the WLS strip with the largest signal and its x neighbors on each side. The reconstructed coordinate is the center of gravity of the selected three (COG1) or five (COG2) WLS strip signals:

$$r_i = \frac{\sum_i x_i \cdot s_i}{\sum_i s_i} \qquad (3.6)$$

x_i is the position of the ith WLS strip, s_i its signal size. Both algorithms need additional strips on each side of the strip with the largest signal, which limits the number of strips with the largest signal to four (COG1) and two (COG2).

The "center of gravity" algorithms have an inherent inaccuracy at the border of two strips. The problem is explained for the COG1 algorithm: assume an event exactly at the border of two strips, e.g. strip 2 and 3. The signal in strip 2 be slightly larger due to statistical fluctuations. The reconstruction algorithm selects strip 2 and its two neighbors 1 and 3. Since the signal in strip 1 is not zero, the reconstructed coordinate is not at the border between strip 2 and 3 but shifted in the direction of strip 1. The shift depends on the ratio between the signal in the strips 2 and 3 and the signal in strip 1. If the signal in strip 3 is slightly larger, the shift goes into the other direction.

A simple correction for this problem is to subtract the smallest selected signal from all selected signals. The improved algorithms are called iCOG1 and iCOG2. For the COG1 algorithm the effect disappears since only two strips are non-zero. For the COG2 algorithm the effect gets smaller but not zero.

3.7.3 Results

As expected, all algorithms show a well visible pattern with a step size of d (figure 28). The measured standard deviation for the maximum algorithm is $\sigma_{rec} = 0.289$ in units of the step size d. This result is identical to the theoretical value $\frac{1}{\sqrt{12}}$.

The "center of gravity" algorithms give standard deviations of $\sigma_{COG1} = 0.109$ and $\sigma_{COG2} = 0.074$. This is a factor three to four smaller than for the maximum algorithm. A far better result is obtained by the improved COG1 algorithm (iCOG1), where the standard deviation is $\sigma_{iCOG1} = 0.004$. The measured standard deviation for the iCOG2 algorithm is $\sigma_{iCOG2} = 0.029$.

3.7.4 Discussion

The measured value is a useful quantity to evaluate the systematic errors of different reconstruction algorithms. It denotes the best possible resolution achievable by an algorithm under the assumption that the statistical fluctuations of the light distribution on the WLS strips was zero.

For the maximum algorithm, the measured values agrees with the theoretical prediction. The maximal resolution using this algorithm is $d \cdot \sigma_{max} = 3.2\,\text{mm} \cdot 0.289 = 0.9\,\text{mm}$. The standard "center of gravity" algorithms allow a better resolution by a factor of four. The improved COG1 algorithm using
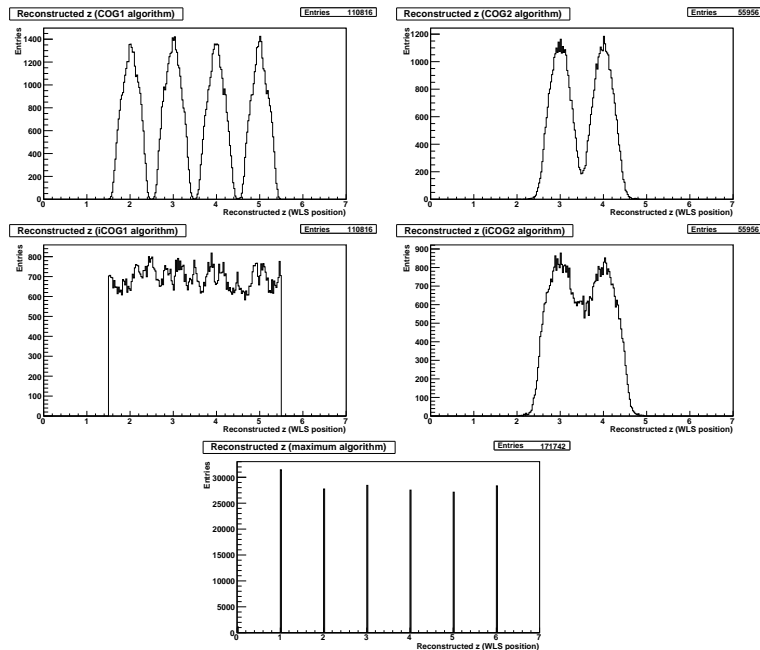
Figure 28: Histograms of the reconstructed coordinates using various reconstruction algorithms. The distribution should be flat because of the isotropic emission of the Na-22 source. Already small systematic errors lead to a well visible structure. The iCOG1 algorithm results in the flattest distribution.

only the largest signal and one neighbor on each side reduces the methodical error to almost zero (0.01 mm). For this method, the dominant limitation in the precision of the coordinate reconstruction is the statistical variation.

## 3.8 Light distribution and single WLS strip light yield

3.8.1 Method

Using the reconstruction algorithms from the previous section, the light distribution on the strips can be examined. For each strip the mean signal size for events at various distances is calculated. The iCOG1-algorithm is used. Since the WLS strip signals are normalized, the peak shapes from several strips can be connected into one peak which covers a wider range of distances.

The maximum of the peak indicates the signal strength in a single WLS strip for events in front of that strip. The number of detected photons per WLS strip can be calculated.

3.8.2 Results

The peak is approximately Gaussian in the inner region, but has a long tail on both sides. The tail is around five detected photons, decreasing with larger
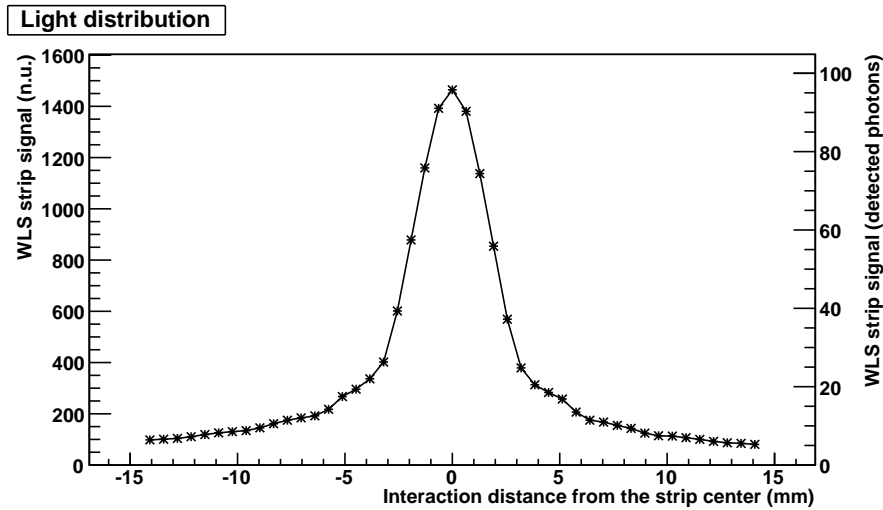
Figure 29: Light distribution in the crystal: the signal strength in a central WLS strip is drawn versus the distance of the events from that strip. The peak maximum is at 96 ± 4 detected photons.

distance of the events from the central WLS strip. Events on top of a strip produce a signal of 1464 n.u., corresponding to 96 ± 4 detected photons.

3.8.3 Discussion

According to a Monte Carlo simulation by P. Solevi (ETH Zurich), the number of optical photons at the MPPC end of the WLS strip is 350. Assuming a photon detection efficiency of 30 % the number of detected photons is 105. By taking into account that this number is in case of a perfect alignment and contact between WLS and MPPC and without light loss due to the distance between diode and chip surface, the measured value of 96 detected photons is in very good agreement with the simulation.

The peak shape also contains the distribution of the (approximately) 182 detected photons in all six strips (section 3.6) on the individual strips: about 96 photons are detected in the central strip. In the two neighboring strips 25 photons are detected each. This is the value of the curve in figure 29 at a distance of 3.2 mm. The next two neighbors contain a signal of about 15 photons each.

3.9 Remark on the determination of the precision of the z-reconstruction

An anticipated result of this setup was the determination of the precision of the z-axis coordinate readout. The measurements made for this purpose are non-conclusive. The chosen method was to position the coincidence crystal at various distances from the Na-22 source, which changes the solid angle of the detected coincidence events of the two crystals. The width of the reconstructed variables in combination with the geometry of the setup in principle contains the precision of the coordinate reconstruction. Due to several reasons the calculation

of the reconstruction precision was not possible. The main problem is that the available geometrical information is not sufficient. On the one hand the exact properties of the Na-22 source are not available. Only the size of the active area is known (1 mm according to the manufacturer). The activity within this area is not uniform and could not be determined.

Furthermore the coincidence crystal is cubic. The length of the divergent photon trajectories within the crystal is not constant over the solid angle where coincidences with the other crystal are possible. This leads to a flattening of the edges in the histogram of the reconstructed coordinates, which makes the extraction of the statistical error almost impossible.

Another approach was to use a lead collimator. The collimator is a lead block of $20 \times 20 \times 30 \, \text{mm}^3$ with a drill hole (diameter 1.5 mm). This solves the problem with the crystal edges. Due to the remaining problem with the source, the available data is not conclusive.

Further measurements with increased distances between source, collimator and crystals would have required a complete reinstallation of the setup which was not possible due to the limited available time.

Acknowledgements

The author wishes to thank the people who provided invaluable help for this diploma thesis. Their work is gratefully acknowledged.

Appendix

A   Light loss through glass window: calculation

A.1   Introduction

This calculation estimates the light loss when the crystal is not attached directly to the diode surface but to a thin glass window glued on the diode surface. The estimation is based on geometrical optics only. The calculation starts in the crystal at the crystal-glass window surface. The optical grease used to improve this contact is neglected since its layer is very thin. The MPPC chip is in a ceramic packaging and coated with silicoloid. The silicoloid is not at the same level as the border of the packaging. The glass plate is laid on the border of the packaging, the space between glass window and silicoloid is filled with optical glue. See graphic 30 for details.

For each point in the contact area the fraction of photons which arrive on the sensitive surface of the MPPC is calculated. Then the integral over the contact area is taken. The ratio of this integral calculated for the cases without and with glass window gives the relative light loss. Four approximations are made:

1. The distribution of the photons is assumed to be homogeneous in the contact area.

2. The angular distribution of the photon directions within the crystal is assumed to be isotropic.

3. The refraction indices of the glass window, glue and silicoloid are similar. For the calculation they are assumed to be identical.

4. A potential angular dependence in the photon detection efficiency of the MPPC is neglected.

A.2   Coordinate system and variable names

A point in the crystals-glass window contact area has the coordinates (a,b), the point of origin being in the middle of the quadratic crystal. The solid angle within the crystal is denoted by Ω_c. The direction of a specific photon is given by φ_c, ϑ_c within the crystal and φ, ϑ outside. The corresponding refraction indices are n_c and n. The coordinates at the chip level are x and y, the chip is at a distance of l from the discontinuity (see figure 30).
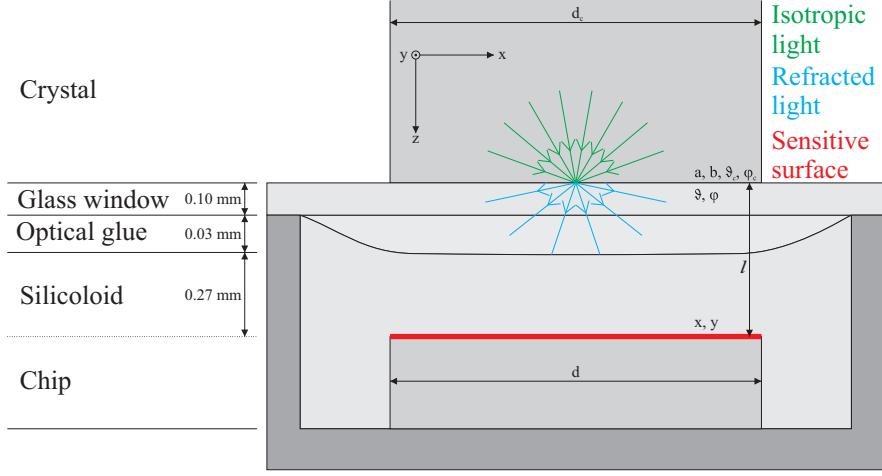
A.3   Calculation

A.3.1   Used formulas

The calculation is based on only two formulas, Snell's law and a coordinate transformation. First Snell's law is written in a differential form to get the relation of $d\vartheta_c$ and $d\vartheta$.

$$n_c sin(\vartheta_c) = n sin(\vartheta) \qquad (A.1)$$
$$n_c cos(\vartheta_c) d\vartheta_c = n cos(\vartheta) d\vartheta \qquad (A.2)$$

Figure 30: Simplified geometry for the calculation (not to scale). Without glass window the crystal is in direct contact with the silicoloid and therefore 0.27 mm away from the sensitive surface. The glass window increases this distance to 0.4 mm.

A coordinate transformation from the coordinates (φ, ϑ, l) to (x, y, l) is necessary. For the integrals in the calculation, the Jacobian M of this transformation has to be calculated.

$$
\begin{aligned}
x &= l\,tan(\vartheta)cos(\varphi) & \text{(A.3)} \\
y &= l\,tan(\vartheta)sin(\varphi) & \text{(A.4)}
\end{aligned}
$$

Two expressions from the inverse transformation are used later:

$$
\begin{aligned}
sin(\vartheta)^2 &= \frac{x^2 + y^2}{l^2 + x^2 + y^2} & \text{(A.5)} \\
cos(\vartheta)^2 &= \frac{l^2}{l^2 + x^2 + y^2} & \text{(A.6)}
\end{aligned}
$$

The Jacobian is given by

$$
\begin{aligned}
M &= \left| \begin{matrix} -l\,tan(\vartheta)sin(\varphi) & \frac{l}{cos(\vartheta)^2}cos(\varphi) \\ l\,tan(\vartheta)cos(\varphi) & \frac{l}{cos(\vartheta)^2}sin(\varphi) \end{matrix} \right| \\
&= \left| l^2 \frac{tan(\vartheta)}{cos(\vartheta)^2}(-sin(\varphi)^2 - cos(\varphi)^2) \right| \\
&= l^2 \frac{sin(\vartheta)}{cos(\vartheta)^3}. & \text{(A.7)}
\end{aligned}
$$

A.3.2 Differential rate after the discontinuity

The differential rate in the glass is given by the (constant) differential rate in the crystal $\frac{dR}{d\Omega_c} \equiv R_0$ and Snell's law. Only one point in the contact area is

considered, the integral over the area is taken later.

$$
\begin{aligned}
\frac{dR}{d\Omega} &= \frac{dR}{d\Omega_c}\frac{d\Omega_c}{d\Omega} \\
&= \frac{dR}{d\Omega_c}\frac{d\varphi_c sin(\vartheta_c)d\vartheta_c}{d\varphi sin(\vartheta)d\vartheta} \\
&= R_0\frac{n^2}{n_c^2}\frac{cos(\vartheta)}{cos(\vartheta_c)} \\
&= R_0\frac{n}{n_c}\frac{cos(\vartheta)}{\sqrt{\frac{n_c^2}{n^2}-sin(\vartheta)^2}}
\end{aligned}
\tag{A.8}
$$

A.3.3 Rate at the sensitive surface

The rate at the sensitive surface of the crystal is the integral over the solid angle $\hat{\Omega}$ which includes the sensitive area. For a given point (a,b) in the contact plane the sensitive surface has the coordinates $[-\frac{d}{2}-a, \frac{d}{2}-a]$ in x-direction and $[-\frac{d}{2}-b, \frac{d}{2}-b]$ in y-direction. The rate $R(a,b,l)$ at the sensitive surface for a point (a,b) in the contact area is

$$
\begin{aligned}
R(a,b,l) &= \int_{\hat{\Omega}}\frac{dR}{d\Omega}d\Omega \\
&= \int_{\hat{\Omega}} R_0\frac{n}{n_c}\frac{cos(\vartheta)}{\sqrt{\frac{n_c^2}{n^2}-sin(\vartheta)^2}}d\varphi \sin\vartheta d\vartheta \\
&= \int_{-\frac{d}{2}-b}^{\frac{d}{2}-b}\int_{-\frac{d}{2}-a}^{\frac{d}{2}-a} R_0\frac{n}{n_c}\frac{\frac{l}{\sqrt{l^2+x^2+y^2}}}{\sqrt{\frac{n_c^2}{n^2}-\frac{x^2+y^2}{l^2+x^2+y^2}}}\underbrace{\frac{l}{(l^2+x^2+y^2)^{\frac{3}{2}}}dxdy}_{d\varphi \sin\vartheta d\vartheta} \\
&= \int_{-\frac{d}{2}-b}^{\frac{d}{2}-b}\int_{-\frac{d}{2}-a}^{\frac{d}{2}-a} R_0\frac{n^2 l^2 dxdy}{n_c(l^2+x^2+y^2)^{\frac{3}{2}}\sqrt{n_c^2 l^2+(n_c^2-n^2)(x^2+y^2)}}
\end{aligned}
\tag{A.9}
$$

A.3.4 Total rate at the sensitive surface

To get the total rate at the sensitive surface, the integral of $R(a,b,l)$ over the contact surface has to be taken. The crystal has a size of d_c in both the a- and b-direction, such that the integral is given by

$$
R(l) = \int_{-\frac{d_c}{2}}^{\frac{d_c}{2}}\int_{-\frac{d_c}{2}}^{\frac{d_c}{2}} R(a,b,l)dadb.
\tag{A.10}
$$

This integral is valid if the crystal is centered relatively to the chip.

A.4 Results

The relative light loss by adding the glass window is $\varepsilon = 1 - R(0.4)/R(0.27)$. All lengths were measured by C. Joram (CERN) using an OGP Smartscope

CNC[9]. The refractive indices are $n_c = 1.8$ for the crystal and $n = 1.5$ for the glass, glue and silicoloid. The crystal and the MPPC chip have the same size, $d_c = d = 3\,\text{mm}$. The integrals are calculated using Mathcad 14. Since Mathcad calculates wrong values for R(a,b,l) when l is small, the calculation is repeated using Mathematica 6. The result is identical: $\varepsilon = 8.8\,\%$.

The function $R(l)$ can be adapted to calculate the light loss due to misalignment of the crystal on the MPPC. This is achieved by adding an offset to the integral boundaries in equation (A.10). The light loss is then $\varepsilon = 1 - R_{\text{off}}(l)/R(l)$ where R_{off} includes the offset. For $l = 0.27$, the light loss is $1.2\,\%$ and $4.4\,\%$ for offsets of 0.1 and 0.2 mm, respectively. For $l = 0.4$ the light loss is smaller ($0.9\,\%$ and $3.3\,\%$).

---

[9]Optical Gaging Products Inc., www.ogpnet.com

References

[1] D. Renker, Nuclear Instruments and Methods in Physics Research Section A: Accelerators, Spectrometers, Detectors and Associated Equipment **571**, 1 (2007).

[2] Hamamatsu Photonics K.K., Japan, *MPPC - Multi-Pixel Photon Counter (Product Specifications)*, 2008.

[3] W. J. Kindt, N. H. Shahrjerdy and H. W. van Zeijl, Sensors and Actuators A: Physical **60**, 98 (1997).

[4] D. Renker, Private communication, 2008.

[5] W. W. Moses, Nuclear Instruments and Methods in Physics Research Section A: Accelerators, Spectrometers, Detectors and Associated Equipment **471**, 209 (2001).

[6] S. R. Cherry and M. E. Phelps, Imaging brain function with positron emission tomography, in *Brain Mapping: The Methods (Second Edition)*, edited by A. W. Toga and J. C. Mazziotta, pp. 485–511, Academic Press, San Diego, 2002.

[7] T. F. Budinger, K. M. Brennan, W. W. Moses and S. E. Derenzo, Nuclear Medicine and Biology **23**, 659 (1996).

[8] A. Braem *et al.*, Nuclear Instruments and Methods in Physics Research Section A: Accelerators, Spectrometers, Detectors and Associated Equipment **580**, 1513 (2007).

[9] J. Séguinot *et al.*, Nuovo Cimento C **029**, 429 (2006).

[10] W.-M. Yao *et al.*, Journal of Physics G **33**, 1+ (2006).

[11] Saint-Gobain Crystals, France, *PreLude 420 LYSO:Ce Scintillation Material (Product Specifications)*, 2004.

[12] I. Vilardi *et al.*, Nuclear Instruments and Methods in Physics Research Section A: Accelerators, Spectrometers, Detectors and Associated Equipment **564**, 506 (2006).

[13] N. N. Ryskin, P. Dorenbos, C. W. E. van Eijk and S. K. Batygov, Journal of Physics: Condensed Matter **6**, 10423 (1994).

[14] C. Pepin *et al.*, Nuclear Science, IEEE Transactions on **51**, 789 (2004).

[15] Saint-Gobain Crystals, France, *BC-842A and BC-484 Wavelength Shifter Bars (Product Specifications)*, 2005.

[16] Texas Instruments Inc., *OPA842 - Wideband, Low Distortion, Unity-Gain Stable, Voltage-Feedback Operational Amplifier*, 2002.

[17] Texas Instruments Inc., *OPA846 - Wideband, Low-Noise, Voltage-Feedback Operational Amplifier*, 2002.

[18] CAEN S.p.A., Italy, *V792 (Technical Information Manual)*, 2007.

[19] P. Solevi, *Study of an in-beam PET system for CNAO, the National Centre for Oncological Hadrontherapy*, PhD thesis, Universita degli Studi di Milano, 2007.

[20] A. Braem *et al.*, Nuclear Instruments and Methods in Physics Research Section A: Accelerators, Spectrometers, Detectors and Associated Equipment **586**, 300 (2008).